International Journal of Biological Macromolecules 332 (2025) 148701

Contents lists available at ScienceDirect

International Journal of Biological Macromolecules

journal homepage: www.elsevier.com/locate/ijbiomac

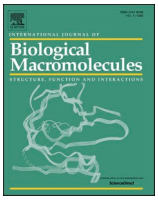

3D printed fibroblast-laden alginate-cellulose scaffolds support extracellular matrix formation and angiogenic growth factor secretion

Jernej Vajda [a,b,*], Dragana Bjelić [c], Boštjan Vihar [a], Matej Vesenjak [d], Polona Dobnik Dubrovski [d], Lidija Gradišnik [a], Monika Belak [a], Uroš Maver [a,b], Marko Milojević [a,b]

[a] University of Maribor, Faculty of Medicine, Institute of Biomedical Sciences, Taborska ulica 8, SI-2000, Maribor, Slovenia
[b] University of Maribor, Faculty of Medicine, Department of Pharmacology, Taborska ulica 8, SI-2000, Maribor, Slovenia
[c] University of Maribor, Faculty of Chemistry and Chemical Engineering, Laboratory for Analytical Chemistry and Industrial Analysis, Smetanova ulica 17, SI-2000, Maribor, Slovenia
[d] University of Maribor, Faculty of Mechanical Engineering, Laboratory for Advanced Engineering Simulations and Experimentation, Smetanova ulica 17, SI-2000 Maribor, Slovenia

ARTICLE INFO

Keywords:
3D bioprinting
Alginate
Cellulose
Skin fibroblast
Microvasculature
Angiogenesis

ABSTRACT

Effective microvascular tissue engineering requires fibroblasts that remain phenotypically stable and secrete extracellular matrix (ECM) proteins and growth factors relevant for vascularization. This study evaluated 3D printed hydrogels based on sodium alginate (ALG) and carboxymethyl cellulose (CMC) to assess their ability to sustain fibroblast phenotype, ECM deposition, and angiogenic growth factor secretion during long-term culture. Seven formulations – including one with nanofibrillated cellulose – were compared by encapsulating fibroblasts and crosslinking with $CaCl_2$ or $SrCl_2$. All scaffolds were printable and exhibited comparable degradation profiles. Mechanical testing indicated stable compressive response, with Sr^{2+}-crosslinked hydrogels generally showing higher apparent compressive modulus, while Ca^{2+}-crosslinked scaffolds supported slightly higher cell viability. Encapsulated fibroblasts retained their phenotype for 30 days, evidenced by steadily increasing collagen I/III and fibronectin deposition, alongside sustained expression of specific fibroblast markers. After 30 days, all groups produced comparable levels of vascular endothelial growth factor (VEGF) and basic fibroblast growth factor (FGF-2), with one formulation yielding a significantly higher FGF-2 output. This multiparametric study demonstrates that scaffold composition and crosslinker chemistry influence fibroblast phenotype maintenance, ECM deposition, and growth factor secretion. To our knowledge, this is the first systematic, 30-day screening of ALG-CMC hydrogels – tuned by polymer content, NFC addition, and Ca^{2+}/Sr^{2+} crosslinking – specifically for their ability to sustain fibroblast phenotype, extracellular matrix deposition, and growth factor secretion, providing design considerations to guide bioink development for microvascular models.

1. Introduction

Tissue engineering is a multidisciplinary field that involves the use of materials, cells, and bioactive molecules to create functional tissues that can replace or repair damaged or diseased tissue [1]. The choice of materials is an important aspect of tissue engineering. Materials used in tissue engineering include natural materials, either animal-derived, such as collagen and fibrin [2,3], or plant-derived, such as alginate and cellulose derivatives [4–6], as well as (semi)synthetic materials [7–9]. These materials serve as scaffolds to provide structural support for cells and to guide tissue growth and organization [10]. Additionally, the same materials can be used to deliver bioactive molecules, such as growth factors, to the cells to promote tissue regeneration [11]. The selection of the appropriate material depends on the targeted engineered tissue and different factors such as the desired mechanical properties, biocompatibility [12] and the ability to deliver bioactive molecules in a controlled manner [13].

Microvascular tissue engineering focuses on creating functional vessel networks, which requires scaffolds that mimic the structural and mechanical properties of native microvasculature [14,15].

* Corresponding author at: University of Maribor, Faculty of Medicine, Taborska ulica 8, 2000, Maribor, Slovenia.
E-mail address: jernej.vajda@um.si (J. Vajda).

https://doi.org/10.1016/j.ijbiomac.2025.148701
Received 3 July 2025; Received in revised form 29 October 2025; Accepted 31 October 2025
Available online 1 November 2025

Endothelial cells are central to angiogenesis, as they sprout from existing vessels, migrate, and form lumens that establish new vascular channels. They also maintain vascular integrity and regulate barrier function and nutrient exchange. Pericytes surround these nascent vessels, providing stability, modulating permeability, and contributing to vascular remodeling and tone [16–19].

Fibroblasts play a crucial role in tissue remodeling by producing extracellular matrix proteins such as collagen and fibronectin, which provide structural support and guide vascular organization [20]. They also secrete cytokines and growth factors, including VEGF and FGF-2, that stimulate endothelial cell function and angiogenesis [21,22]. Through these activities, fibroblasts coordinate with endothelial cells and pericytes to stabilize and mature microvascular networks. When fibroblast activity is impaired, ECM assembly is compromised, vessel maturation is delayed, and nutrient and oxygen delivery to tissues is reduced [23–25].

Therefore, it is vital in microvascular tissue engineering to utilize materials that are biocompatible with fibroblasts and maintain relevant interaction, attachment, and functionality of fibroblasts.

Animal-derived materials such as collagen, fibrin, and other ECM materials have been traditionally used as scaffold materials in microvascular tissue engineering [2,3]. However, they are not ideal due to the potential for immune rejection [26], the risk of disease transmission [27,28], ethical concerns [29] and price, especially in high-grade products with suitable certificates [30]. Plant-derived materials have emerged as a promising alternative to animal-derived materials in microvascular tissue engineering [31]. Materials such as cellulose [32], xylan [33], and lignin [34], have similar mechanical properties to ECM and can be chemically modified to also mimic other desired ECM properties [35]. Furthermore, plant-derived materials are biocompatible, non-immunogenic, and can often be easily obtained in large quantities. Additionally, they are mostly less expensive than animal-derived materials and can be produced sustainably [36].

Both sodium alginate (ALG) and carboxymethyl cellulose (CMC) are frequently employed in tissue engineering and have been proven to be fibroblast-friendly [37,38]. These materials have several benefits, including the capacity to encapsulate cells, ease of gelation, and biodegradability. ALG-based bioinks are widely used due to their mild gelation with divalent ions and ease of processing [39–41]. Blending with cellulose derivatives such as CMC or NFC improves viscosity, shear-thinning behavior, and print fidelity [42]. In contrast, CMC can form a physical gel through self-association of the polymer chains, which relies on interactions like hydrogen bonding and entanglements between polymer chains to create a gel-like structure, without the need for chemical reactions [43–45]. Both substances offer a favorable milieu for cell adhesion, growth, and migration [43–45]. However, a variety of variables, including concentration, crosslinking technique, mechanical properties, degradation properties, and interactions with other elements of the tissue engineering construct, might affect how biocompatible a given material is [14].

The ionic crosslinking of ALG and CMC is a primary determinant of scaffold structure, stability, and mechanics. The identity of the divalent cation modulates network architecture, elasticity, swelling, and degradation kinetics [46,47]. Although Ca^{2+} is widely used due to predictable gelation, Sr^{2+} and other divalent ions can produce measurably different gel properties, motivating direct comparison in cell-laden constructs [41,48]. Beyond static stiffness, time-dependent viscoelasticity of alginate matrices also regulates cell behavior, underscoring the need to evaluate how composition and crosslinking agent choice affect long-term function [49].

Because of its unique properties and biocompatibility, nanofibrillated cellulose (NFC) has shown significant promise for tissue engineering. NFC, which is derived from organic cellulose sources like wood pulp or plant fibers, has a big surface area and robust mechanical characteristics at the nanoscale [46,47]. Because NFC forms a three-dimensional (3D) structure that closely matches the ECM of natural tissues, it is an excellent scaffold material for tissue engineering [50]. Its ability to transfer nutrients and oxygen effectively at the nanoscale helps in cell adhesion, proliferation, and differentiation [51]. Moreover, the biodegradability of NFC ensures that the scaffold will gradually break down over time, concurring with the growth of new tissue [51]. This sustainable and regenerative biomaterial has been studied for a wide range of applications, including cartilage, bone, and skin regeneration. Because of its eco-friendliness and capacity to sustain biological functions, NFC presents itself as a viable option for advancing tissue engineering [50,51].

Despite the importance of fibroblast-matrix interactions, most studies on fibroblast-laden hydrogels have been short-term or have varied only a single parameter, such as alginate concentration or type of crosslinking agent. Systematic, long-term, multiparametric comparisons that combine different ALG-CMC compositions, nanofibrillated cellulose addition, and Ca^{2+} versus Sr^{2+} crosslinking, remain limited. We hypothesize that specific ALG-CMC composite scaffolds support the maintenance of fibroblast phenotype and stimulate extracellular matrix deposition and secretion of angiogenic growth factors during 30 days of in vitro culture. To test this, we performed a multiparametric evaluation of seven formulations, assessing printability, degradation, mechanical response, and fibroblast compatibility. Our overall concept and motivation are presented in Fig. 1. In the scope of this manuscript, as depicted in the highlighted part of the figure, the ECM and growth factor production by fibroblasts were assessed when culturing them in scaffolds with different material compositions.

2. Materials and Methods

Schematic representation of the formulations, materials, and subsequent techniques and their effect on material selection is presented in Fig. 2. Note, the formulations are hydrogels composed of different concentrations of polymers, and the materials are these formulations after having been crosslinked with either of the crosslinking agents.

2.1. Cell sources

Human skin fibroblasts – ATCC CCL-110™ Detroit 551 (HSF) were used throughout the study.

Base culture of HSF cells was maintained in Advanced Dulbecco's Modified Eagle's Medium (ADMEM, Gibco, Thermo Scientific, Waltham, MA, USA), supplemented with 5 *v*/v% fetal bovine serum (FBS, Gibco, Thermo Scientific, Waltham, MA, USA), at 37 °C and 5 % CO_2.

2.2. Preparing the formulations

First, 7 different hydrogel formulations were prepared using sodium alginate (ALG, Mw: 80 kDa, CAS num.: 9005-38-3, Sigma-Aldrich, Darmstadt, Germany) and carboxymethyl cellulose (CMC, in the form of sodium salt, Mw: 700 kDa, degree of substitution of 0.9, CAS num.: 9004-32-4, Sigma-Aldrich, Darmstadt, Germany), dissolved in ultrapure water (18.2 MΩ·cm at 25 °C), prepared using an ELGA Purelab water purification system (Veolia Water Technologies, HighWycombe, UK). One formulation also incorporated nanofibrillated cellulose (NFC, purchased from The Process Development Center, University of Maine (Orono, Maine, USA)).

It should be noted that all the percentages of ALG, CMC, and NFC throughout the article are weight percentages – w/w.

The formulations were as follows: formulation A (7 % ALG and 3 % CMC), formulation B (1 % ALG and 5 % CMC), formulation C (3 % ALG and 5 % CMC), formulation D (5 % ALG and 5 % CMC), formulation E (1 % ALG and 7 % CMC), formulation F (3 % ALG and 7 % CMC), and formulation G (5 % ALG and 5 % CMC and 1.5 % NFC), as depicted in Fig. 2.

The gels were homogenized using an overhead mixer and then stored for 24 h at 8 °C before 3D printing.

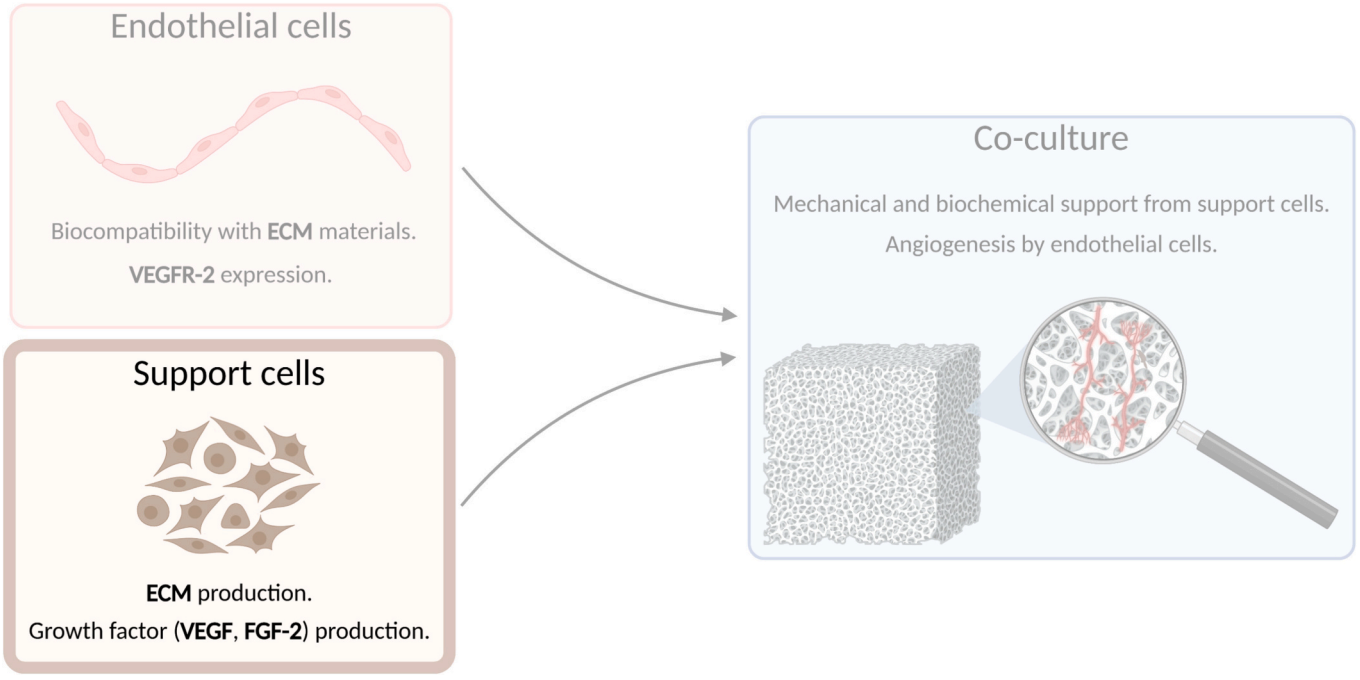

Fig. 1. The concept of our work with the scope of this article in the highlighted part of the figure.

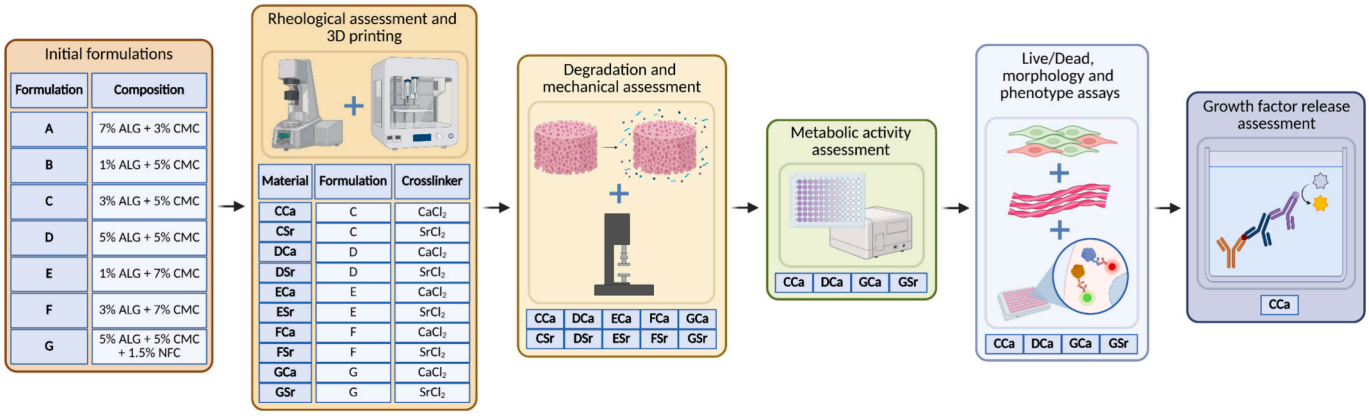

Fig. 2. Schematic representation of the formulations, materials, and subsequent techniques and their effect on material selection. The figure presents the overall workflow of the study, illustrating the successive experimental steps, the designation of sample names, and the progressive selection and filtering of materials that led to the identification of the optimal formulation.

2.2.1. *Rheology testing of the gels*

Prior to printing, viscosity was measured for all base formulations. All measurements were performed with an RheolabQC rheometer (Anton Paar GmbH, Graz, Austria) with cylinder measurement system CC27-SN25789 according to the ISO 3219 standard. During the measurements, the temperature was kept constant at 25 °C and the shear rate (Γ) was increased continuously from 0.01 to 1000 s^{-1} with 31 measuring points at every 10 s for a total duration of 310 s. The analysis method and curve fitting according to Carreau-Yasuda [52,53] was used.

2.2.2. *3D printing of scaffolds*

The first phase was 3D printing the scaffolds using each of the formulations. The scaffold structure design was created using our in-house developed scaffold generator software, accessible online [54]. Cuboid scaffolds with dimensions of 12 (L) × 12 (W) × 2.5 (H) mm^3 were fabricated using the Vitaprint 3 bioprinter (IRNAS d.o.o., Maribor, Slovenia) and conical, blunt-end extrusion nozzles (Nordson EFD, Westlake, OH, USA) with an inner diameter of 0.25 mm.

Polycaprolactone (PCL) scaffolds for controls used in resazurin reduction assay were fabricated using Vitaprint 3 (IRNAS d.o.o., Maribor, Slovenia) bioprinter and in-house custom-made stainless-steel cartridge and aluminum extrusion nozzle with an inner diameter of 0.25 mm at a nozzle temperature of 80 °C. PCL used was purchased from Sigma-Aldrich, Darmstadt, Germany.

2.2.3. *Crosslinking of the scaffolds*

The scaffolds were crosslinked 3 min post-printing with either 5 wt% calcium chloride ($CaCl_2$) or 5 wt% strontium chloride ($SrCl_2$), both purchased from Sigma-Aldrich, Darmstadt, Germany. The scaffolds were completely covered and left in the solution for 1 min. The crosslinked scaffolds were frozen at −80 °C and then lyophilized. To be sterilized before use, the scaffolds were treated with a UV light from both sides, 30 min for each side.

After crosslinking them with either $CaCl_2$ or SrCl2, the scaffolds were assigned the designation by combining the formulation (C/D/E/F/G) and the crosslinking agent ($CaCl_2$/$SrCl_2$), thus obtaining the scaffold

designations, presented in Fig. 2 above.

2.3. Mechanical properties of the scaffolds

2.3.1. In vitro scaffold degradation testing

The second phase was testing the formulations for degradation properties. All scaffolds were weighed in their lyophilized state (W_0). Scaffolds were then submerged in ADMEM +5 *v*/v% FBS and incubated at 37 °C and 5 % CO_2. There were 5 planned timepoints in degradation experiments: 1 day, 3 days, 7 days, 14 days, and 21 days. Each combination of formulation and crosslinking agent had triplicates for each timepoint, totaling 180 scaffolds. At each timepoint, the three replicate scaffolds of each combination were removed from the medium, frozen at −80 °C, lyophilized, and weighed.

2.3.2. Mechanical compression testing

The mechanical behavior of scaffolds subjected to different degradation intervals was also analyzed by experimental testing. For this purpose, quasi-static compressive tests were performed using the Tinius Olsen testing machine H10KT (Tinius Olsen, Redhill, UK) with compressive plates [55]. The specimens were inserted between compressive plates and loaded with a constant loading velocity of 2 mm/min. The loading velocity corresponds to an engineering strain rate of $<0.02\ s^{-1}$. An overview of the specimens and the number of tested specimens is given in Table 1.

To evaluate the mechanical behavior of tested specimens, the force and displacement of the loading plate were monitored and recorded. From the measurements and the scaffold dimensions, strain and stress were calculated. Due to the low thickness of the specimens, the deformation mechanism was not observed.

2.3.3. Morphological characterization by nano-CT

Lyophilized scaffolds were analyzed using high-resolution nano-computed tomography (nano-CT, Zeiss Xradia 620 Versa, Carl Zeiss Microscopy, Pleasanton, USA) at 0.4× and 4× magnification with an isotropic voxel size of 27.758 μm and 2.7382 μm, respectively, operated at 80 kV and 125 μA in both cases. Image reconstruction was performed using the instrument's integrated software. Volumetric datasets were imported into Dragonfly 3D World (Object Research Systems, Montreal, Canada) for segmentation and analysis. Quantitative metrics included pore volume, pore surface area (Lindblad 2005 model), pore sphericity, and strand diameter.

2.4. Material biocompatibility testing

Biocompatibility was assessed using two methods: Live/Dead cell viability assay and Alamar Blue quantitative cell viability and proliferation assay.

2.4.1. Resazurin reduction assay

The alamarBlue™ Cell Viability Reagent (Thermo Fisher Scientific Inc., Waltham, MA, USA) was used to quantify the relative metabolic activity of all four cell types on their respective materials. It is a fluorescent assay that detects cellular metabolic activity. The blue, non-fluorescent reagent 7-hydroxy-10-oxidophenoxazin-10-ium-3-one (resazurin) is reduced to highly fluorescent 7-hydroxy-3H-phenoxazin-3-one (resorufin) by dehydrogenase enzymes in metabolically active cells. This conversion occurs only in viable cells, and therefore, the amount of resorufin produced is proportional to the number of viable cells in the scaffold. The readily soluble resorufin can be easily quantified using the Varioskan multiplate reader (Thermo Fisher Scientific Inc., Waltham, MA, USA) by measuring fluorescence intensity at an excitation wavelength of 530 nm and emission wavelength of 590 nm [56].

The scaffolds in their lyophilized state were submerged in ADMEM +5 *v*/v% FBS on a 24-well plate and incubated without cells at 37 °C and 5 % CO_2 for 24 h to achieve their wet state. Then, the remaining medium was removed and the cells were seeded onto the scaffold using a pipette – a 50 μl drop with 50,000 cells was carefully distributed over the scaffold. After 6 h, the remaining medium was added to the wells.

After 72 h of culture, the Resazurin reduction assay was performed as per manufacturer's protocol.

2.4.2. Live/dead assay

The Live/Dead assay (Biotium, Inc., Fremont, CA, USA) was used to qualitatively assess the influence of different materials on the cell viability of different cell types. Viable cells are detected by the presence of intracellular esterase activity, which converts plasma membrane-permeable calcein-AM to calcein and produces green fluorescence. Dead cells are detected by ethidium homodimer III, which enters the cells through the damaged plasma membrane and intercalates with the DNA double helix to emit red fluorescence. Cells stained in this manner were observed directly on the scaffold surface under a fluorescence microscope (EVOS, FL Cell Imaging System, Thermo Fisher Scientific Inc., Waltham, MA, USA) [57].

The samples were prepared as in Section 2.4.1.

After 72 h of culture, the culture medium was removed from the wells, and cell-seeded scaffolds were washed with FBS-free medium three times. Then, the Live/Dead assay was performed as per the manufacturer's protocol.

2.5. Morphology assessment with cytoskeleton staining

Cytoskeleton staining was used to evaluate the potential influence the materials might have had on the HSF cells' morphology. This was determined through dyeing of the cell cytoskeleton (F-actin fibers) using Phalloidin – Alexa Fluor Plus 555 Phalloidin (Thermo Fisher Scientific Inc., Waltham, MA, USA).

The bioinks were prepared by incorporating skin fibroblasts into the hydrogels, with the best results from previous assays – CCa, DCa, GCa, and GSr were selected for this phase. First, more concentrated gels were prepared, and then the cell solution was added to the gel, resulting in the same gel concentrations as previously, but this time using cell culture medium instead of water. Using those four bioinks, $7 \times 7 \times 7\ mm^3$ scaffolds were 3D printed and put in 24-well plates with 2 ml of cell culture medium per well.

The scaffolds were first fixed in 4 % paraformaldehyde and then submerged in tissue freezing medium overnight. The next day, the specimens were frozen, and 50 μm cryosections were made using Cryostar NX50 (Epredia, PHC Group, Thermo Fisher Scientific Inc., Waltham, MA, USA). The acquired cryosections with HSF cells were washed three times with PBS.

The cell structure was assessed by staining F-actin fibers with phalloidin. All the testing was performed in a dark room. The final step was the addition of the Fluoroshield Mounting Medium with 4′,6-diamidino-2-phenylindole (DAPI, Sigma-Aldrich, Darmstadt, Germany) to dye the cell nuclei. Examination of the stained cells was performed at the required wavelengths for the respective dyes (excitation/emission: DAPI = 306/460 nm, Phalloidin = 556/574 nm). All micrographs were acquired using the EVOS FL Cell Imaging System (Thermo Fisher Scientific Inc., Waltham, MA, USA) [57].

Table 1
Overview of the tested specimens.

Specimens					Degradation intervals [days]	Number of specimens
CCa CSr	DCa DSr	ECa ESr	FCa FSr	GCa GSr	1, 3, 7, 14, 21	3 multiplicates for each specimen and degradation interval, 150 in total

2.6. Functional cell properties in contact with the formulations

2.6.1. Phenotype retention testing over 30 days

ICC staining was used to assess the cells' phenotype retention over 30 days of culturing on the materials. The samples were prepared as in the Section 2.4.1. Over the 30 days, the cell culture medium was replaced every 3–4 days. The acquired cryosections with HSF cells were washed three times with PBS. The general protocol provided by the manufacturer to perform ICC followed. The cryosections were stained using Anti-S100A4 (fibroblast specific protein (FSP-1) [58]) antibody (ab196168, Abcam, Cambridge, UK) at a dilution of 1:100, Anti-Fibroblasts (TE-7) antibody (cbl271, Sigma-Aldrich, Darmstadt, Germany) at a dilution of 1:60, and Anti-Vimentin antibody (ab195877, Abcam, Cambridge, UK) at a dilution of 1:1000; FSP-1 and vimentin were both stained with conjugated antibodies while TE-7 required additional secondary Anti-Mouse antibody (ab150113, Abcam, Cambridge, UK) at a dilution of 1:200. All the testing was performed in a dark room. The final step was the addition of the Fluoroshield Mounting Medium with DAPI (Sigma-Aldrich, Darmstadt, Germany) to dye the cell nuclei. Examination of the stained cells was performed at the required wavelengths for the respective dyes (excitation/emission: DAPI = 306/460 nm, Anti-S100A4 = 650/671 nm, Anti-Fibroblasts (TE-7) = 488/525 nm, Anti-Vimentin = 488/525 nm). All micrographs were acquired using the EVOS FL Cell Imaging System (Thermo Fisher Scientific Inc., Waltham, MA, USA).

2.6.2. Measurement of structural and functional proteins

ICC staining was used to assess the cells' production of structural and functional proteins collagen I, collagen III, and fibronectin. First, preliminary testing was performed to assess how the three proteins were expressed in monolayer culture after 3 days of culture. The samples were then prepared as in Section 2.4.1. During the 30 days of the experiment, the cell culture medium was replaced every 3–4 days. The acquired cryosections with HSF cells were washed three times with PBS. The general protocol provided by the manufacturer to perform ICC followed. The cryosections were stained using Anti-Collagen I antibody (ab138492, Abcam, Cambridge, UK) at a dilution of 1:2000 (corresponding to a concentration of 0.44 μg/ml), Anti-Collagen III alpha 1 antibody (nb600–594, Novusbio, Littleton, CO, USA) at a dilution of 1:100, and Anti-Fibronectin antibody (ab198933, Abcam, Cambridge, UK) at a dilution of 1:100; fibronectin was stained with conjugated antibodies while collagen I and collagen III required additional secondary Anti-Rabbit antibody (ab150077, Abcam, Cambridge, UK) at a dilution of 1:200. All the testing was performed in a dark room. Examination of the stained cells was performed at the required wavelengths (excitation/emission = 488/525 nm). All micrographs were acquired using the EVOS FL Cell Imaging System (Thermo Fisher Scientific Inc., Waltham, MA, USA).

Quantification of ECM protein production was performed in FIJI (ImageJ 1.54p) on native 16-bit images acquired under identical exposure and gain settings. A fixed ROIs of identical size and position were applied across all samples to ensure comparability, and background subtraction was applied. Then, mean gray values were recorded for each scaffold and timepoint. Values are presented as relative fluorescence intensity in bar graphs alongside representative images. For each scaffold group and timepoint, five representative fields were analyzed across independent scaffolds ($n = 2$ scaffolds per group, five fields per scaffold). Mean gray value was measured for each ROI, and results are reported as relative fluorescence intensity in arbitrary units (a.u.), mean ± SD.

2.6.3. Growth factor release measurements with ELISA

The bioink scaffolds were prepared as in Section 2.4.1. Growth factor release was measured in the cell culture medium in 24-well plates with submerged bioink scaffolds. Fibroblast growth factor 2 (FGF-2; also, bFGF – basic fibroblast growth factor) and vascular endothelial growth factor (VEGF) concentrations were measured in cell culture medium using ELISA, both assay kits purchased from Abcam, Cambridge, UK (ab99979 and ab222510). There were 4 planned timepoints of the experiment: 0 days, 3 days, 7 days, and 30 days. The cell culture medium was always replaced exactly 72 h before taking samples, except for the first timepoint where the cell culture medium was 6 h in the culture. The medium samples were taken and immediately frozen at −20 °C until the end of sampling. Then, the samples were thawed, and an ELISA assay was performed on all the samples at the same time.

2.7. Statistical analysis

All numerical values are reported as mean with standard deviation (SD). The Shapiro–Wilk test confirmed the normal distribution of the experimental data. Levene's test was used to assess the equality of variances. As all data sets were well-modeled by a normal distribution and homoscedastic, a one-way analysis of variance (ANOVA), performed within each endpoint and timepoint, followed by the Bonferroni-corrected post-hoc test, was carried out accordingly. For experiments with repeated sampling over time, each timepoint was analyzed independently; multiplicity control (Bonferroni) was applied within that timepoint family of pairwise comparisons. Obtained (Bonferroni-adjusted) p-values <0.05 were considered statistically significant (two-sided). Statistical analysis was performed using IBM SPPS Statistics 27 (IBM Corp. Armonk, NY, USA). For the material biocompatibility (Alamar Blue) endpoint and the ELISA endpoints (VEGF, FGF-2), we additionally report 95 % confidence intervals (CIs) for group means and for selected pairwise mean differences at the key comparisons referenced in the Results.

2.8. Ethical considerations

This study used commercially available human skin fibroblasts (ATCC CCL-110™, Detroit 551). As the cells are established lines obtained from a certified provider and do not contain identifiable donor information, institutional review board approval was not required under local policy.

3. Results and discussion

It should be noted that for Sections 3.3, 3.4, and 3.5, where cryosections were used for staining, 6 multiplicates of each sample at different Z-planes were assessed and did not show visible differences so only one of each was selected for the manuscript.

3.1. Preparing the materials and 3D printing of scaffolds

To shed more light on the rheological properties that might affect the

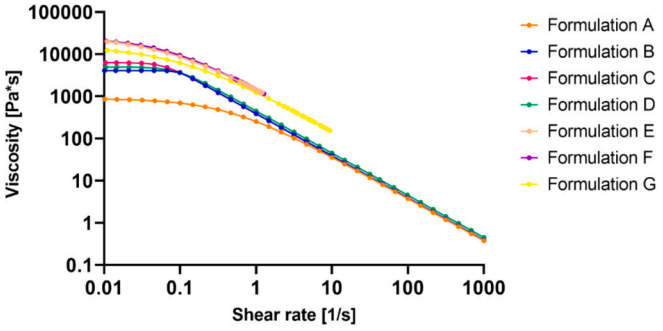

Fig. 3. Viscosity curves of formulations A–G measured with an Anton Paar RheolabQC rheometer (CC27 system) at 25 °C. Shear rate was increased from 0.01 to 1000 s^{-1}, showing shear-thinning behavior in all groups. Formulations with higher CMC content exhibited higher zero-shear viscosity, and NFC addition (formulation G) substantially increased viscosity.

3D printing process, the flow properties of the developed formulations before printing were analyzed (shown in Fig. 3).

For all the obtained formulations, the results show shear-thinning properties of all the samples. The flow curves differ significantly between certain formulations; note the scale of the vertical axis at each of the measurements.

In general, formulations containing more CMC showed higher viscosity when compared to formulations containing more ALG. This can be clearly seen when comparing formulations A and F which have the same total polysaccharide content but with inverted ALG and CMC concentrations (A – 7 % ALG and 3 % CMC, F – 3 % ALG and 7 % CMC).

Comparing formulations D and G, it can also be observed that the addition of NFC increases the viscosity of the hydrogel substantially, with zero shear viscosity equaling 4950 Pa·s and 15,400 Pa·s, respectively.

Although all formulation showed shear-thinning properties, two formulations (A and B) did not prove suitable for 3D printing as they were not viscous enough in static conditions, leading to the rapid collapse of the geometry post-printing. Fig. 4 shows formulations A and B at different timestamps after printing, which clearly shows scaffolds collapsing after as little as 3 min. The other formulations (C, D, E, F, G) were stable enough for 3D printing and were used in further tests. This can be further supported by viscosity measurements where A and B show lower viscosities. See Fig. 3.

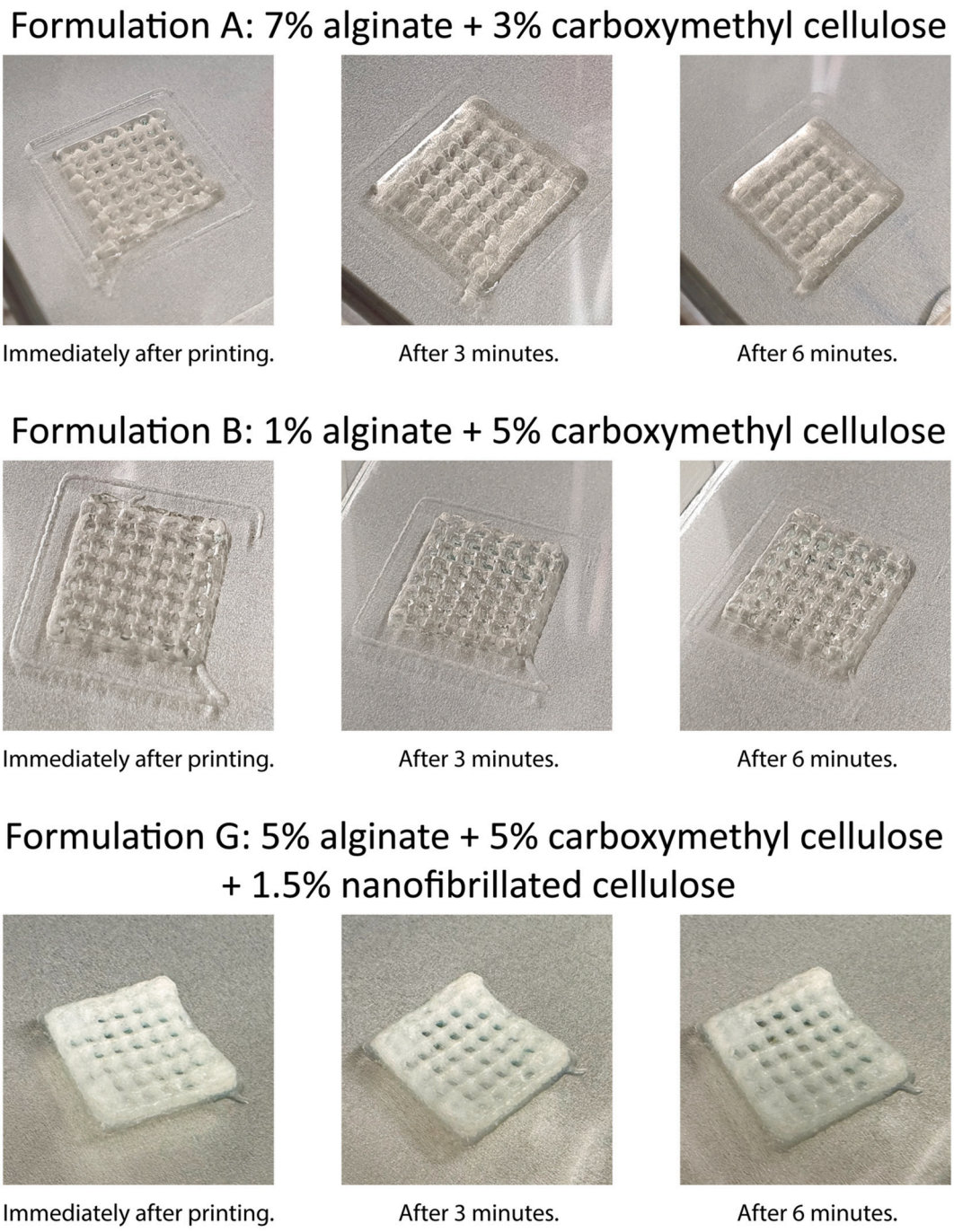

Fig. 4. Representative images of scaffolds printed with formulations A, B, and G, showing structural collapse within minutes after printing with formulations A and B, and structural stability with formulation G. Each scaffold footprint measured 12 × 12 mm^2. Images were taken at different timepoints post-printing using a camera. Formulations A and B were excluded from further testing due to insufficient shape fidelity.

The remaining formulations C, D, E, F, and G were used to 3D print the scaffolds.

3.2. Mechanical properties of the scaffolds

For a scaffold material to be suitable for tissue engineering, it must withstand the conditions in which it will be used, and for a long enough time, depending on the intended use case. To allow direct comparison, all degradation and mechanical data are presented together in Fig. 5 below. The multipanel format facilitates side-by-side evaluation of degradation effects, crosslinker choice, and NFC incorporation within a unified visual framework. Fig. 5A shows the in vitro degradation of the scaffolds at different time intervals. The results are presented as a relative mass loss compared to the lyophilized mass at the beginning of the experiment. They show that all the materials perform similarly and neither of them degrades significantly after 3 weeks of being incubated in a cell culture medium.

The plots in Fig. 5A show the relative weight retention of the

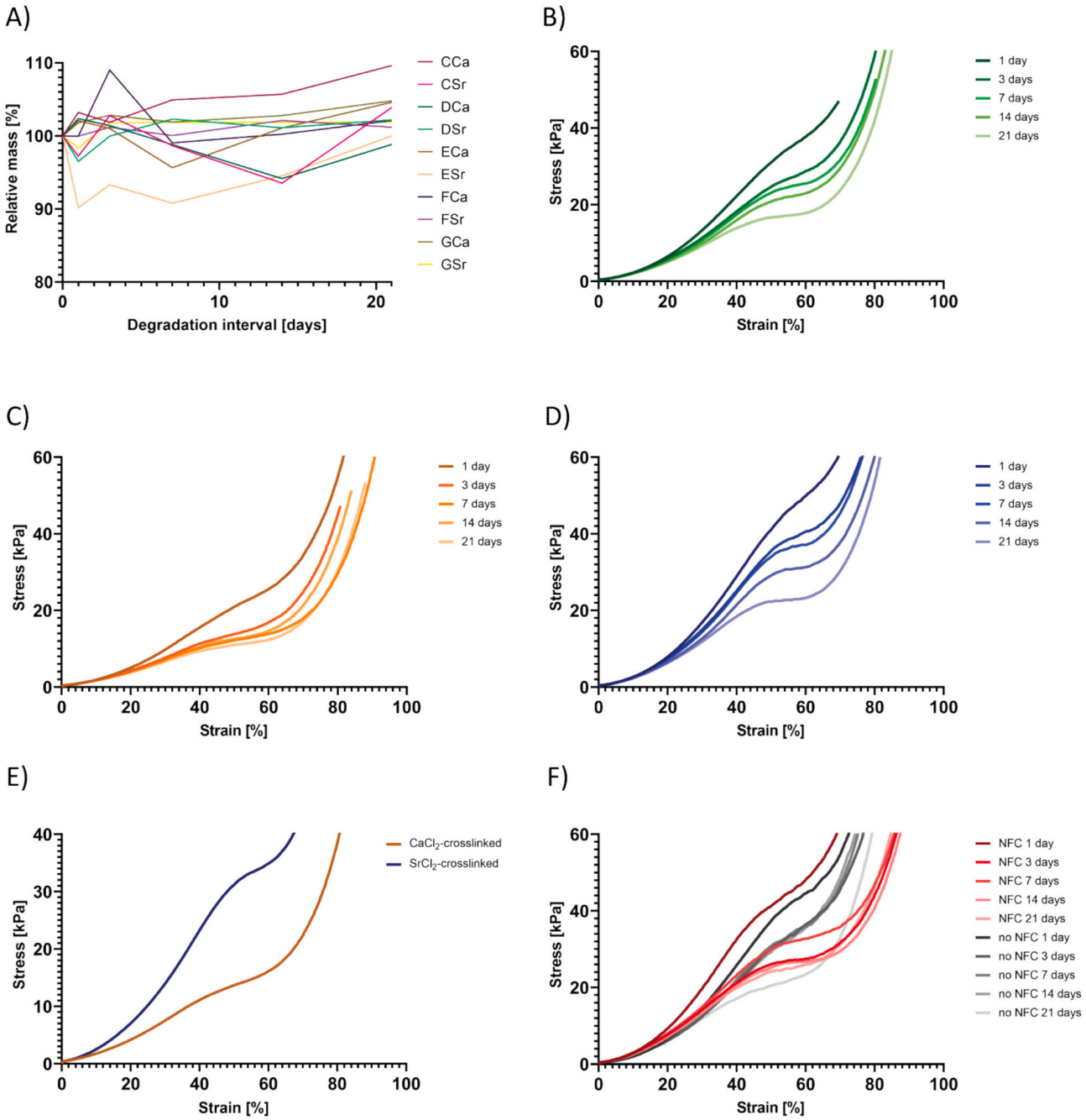

Fig. 5. Scaffold degradation and mechanical properties. **A)** Relative mass retention over 21 days in culture medium ($n = 3$ per condition). **B)** Influence of degradation on mechanical behavior. **C)** Influence of degradation on the mechanical behavior of specimens crosslinked with $CaCl_2$. **D)** Influence of degradation on the mechanical behavior of specimens crosslinked with $SrCl_2$. **E)** Averaged comparison of mechanical responses between the specimens crosslinked with $CaCl_2$ (CCa, DCa, ECa, FCa, GCa) and those crosslinked with $SrCl_2$ (CSr, DSr, ESr, FSr, GSr). **F)** Influence of the incorporation of NFC on compressive behavior. D and G formulations had the same composition with the only difference of adding NFC to the G formulation. "NFC" in the graph legend denotes the average of all the DCa and DSr samples, while "no NFC" denotes the average of all the GCa and GSr samples. | Mechanical properties were evaluated by quasi-static compression at 2 mm/min. Representative curves are shown; full numerical values of apparent compressive modulus and plateau stress are reported in Supplementary Information.

lyophilized scaffolds at each timepoint during degradation. All the scaffolds exhibited similar degradation profiles and retained their weight for up to 21 days under cell culture conditions. It is interesting to note that the weight of the scaffolds increased during the first few days (and even up to 21 days in some cases). We hypothesize that this is due to specific solutes (e.g., proteins) from the cell culture medium being deposited and adhering to the material of the scaffolds.

Furthermore, the influence of degradation time, crosslinking agent, and incorporation of NFC on mechanical properties was evaluated by compression tests. The tests were performed in the absence of cells, as they could hinder the assessment of the difference between the materials, and in case of their presence, it could lead to unforeseen heterogeneity between the samples and increased variability, as stated by previous studies [59–61]. The average mechanical responses of specimens being submerged in a cell medium for different periods are shown in Fig. 5B. From the stress–strain curves, it can be observed that the initial compressive stress–strain response was similar for all specimens up to ~20 % strain, regardless of the duration of submersion. The apparent compressive modulus remained stable until ~45 % strain, after which the curves showed either a plateau or sharp stress increase depending on crosslinking agent and degradation time. However, the apparent compressive modulus drops consistently with increasing the duration of submersion. While the stress progressively increases in the case of specimens submerged in cell medium for 1 day, a stress plateau starts forming in scaffolds submerged for a longer time period. At approx. 60 % strain, the stress starts to increase drastically in all the specimens.

The diagrams in Fig. 5C **and** Fig. 5D show the mechanical response of specimens crosslinked with $CaCl_2$ and $SrCl_2$ being submerged in a cell medium for different periods. The response corresponds to the mechanical behavior described above. It can be observed that the apparent compressive modulus of the specimens decreases by increasing the duration of submersion. However, a difference in mechanical response between the specimens crosslinked with $CaCl_2$ and $SrCl_2$ can be observed. The apparent compressive modulus of the specimens crosslinked with $CaCl_2$ drops significantly after a 1-day submersion, then the apparent compressive modulus stabilizes – the apparent compressive modulus still drops with increasing submersion duration, albeit only slightly. A similar result, although on different formulations, was observed in our previous study [57]. A different mechanical behavior can be observed in the case of specimens crosslinked with $SrCl_2$ – the apparent compressive modulus decreased progressively with increasing the submersion duration.

The responses obtained of tested specimens at different durations of submersion have been averaged to compare the mechanical response of specimens crosslinked with $CaCl_2$ and $SrCl_2$. In Fig. 5E, it can be observed that the specimens crosslinked with $SrCl_2$ exhibit a significantly higher apparent compressive modulus in comparison to specimens crosslinked with $CaCl_2$. Consistent with prior work, L-guluronic acid (G-) blocks in alginate display higher binding affinity for Sr^{2+} than for Ca^{2+} [62], and our previous data align with this trend [57]. Accordingly, the higher apparent compressive modulus observed for $SrCl_2$-crosslinked specimens is most plausibly explained by differences in cation–alginate binding affinity and the resulting crosslink stability under culture conditions. In addition, classic studies indicate that Ca^{2+} shows lower selectivity in ion-exchange affinity than Sr^{2+} when competing with monovalent ions [63], which could contribute to faster exchange of Ca^{2+} in the medium and a more rapid reduction in mechanical response. We emphasize that we did not directly quantify crosslink density or ion-exchange kinetics here; these mechanistic statements are presented as plausible explanations consistent with the literature rather than definitive proof. In the case of specimens crosslinked with $SrCl_2$, the stress initially continuously increases until approx. 40 % strain, then the steepness of the curve decreases, and then starts to increase further at strain above 50 %. In the case of specimens crosslinked with $CaCl_2$, the stress almost linearly increases until approx. 55 % strain, after which the stress starts to increase more steeply.

The influence of NFC incorporation on the compressive behavior of specimens submerged in cell medium for different time periods is shown in Fig. 5F. In both cases (with and without NFC incorporation), the apparent compressive modulus of the specimens drops significantly after exceeding the submersion duration of 1 day. This effect is even more pronounced in scaffolds containing NFC. However, the apparent compressive modulus of NFC-containing scaffolds stabilizes after 3 days and does not decrease further with prolonged submersion. This was not confirmed for the case of specimens without NFC, suggesting that the incorporation of NFC decreases short-term and increases long-term mechanical stability.

Full numerical values corresponding to Fig. 5A–F are provided in *Supplementary Information*.

The microstructure of the bioinks and their interfacial characteristics were further evaluated through high-resolution nano-CT analysis, which provided quantitative, three-dimensional information on the internal architecture of the printed scaffolds. This approach enabled a detailed assessment of pore geometry, connectivity, and filament arrangement throughout the entire scaffold volume. Nano-CT imaging of lyophilized scaffolds preserves the overall three-dimensional organization of the structure and allows volumetric analysis of the pore morphology, offering a representative view of the scaffold internal structure and organization relevant for nutrient diffusion, fibroblast infiltration, and overall construct stability. For these reasons, nano-CT was selected as the primary tool for microstructural characterization, providing quantitative data that directly supports the interpretation of fibroblast behavior within the scaffolds. At low magnification (0.4×), the nano-CT reconstructions revealed a highly ordered print geometry with continuous filament deposition (Fig. 6A). Higher-magnification scans (4×) showed well-connected pore networks and smooth filament junctions, confirming print fidelity and consistent crosslinking throughout the construct (Fig. 6B). Three-dimensional segmentation of the pore space (Fig. 6C) illustrated a heterogeneous but interconnected porosity, with individual pores ranging from tens to several hundred micrometers. Skeletonization of the strand network (Fig. 6D) highlighted the continuity and branching of the filaments, indicating a balance between mechanical stability and mass-transport pathways. Quantitative morphometric analysis supported these observations: the mean pore volume was 320,656 μm^3, mean pore surface area (Lindblad 2005 model) was 24,123 μm^2, and mean Feret diameter was 74.4 μm, dimensions favorable for fibroblast infiltration and nutrient diffusion [64]. The mean pore sphericity of 0.769 indicated predominantly rounded pore geometries rather than elongated voids ($n = 1057$). Strand morphology analysis showed filaments narrower than the surrounding voids, with an average diameter of 20.96 μm. These features together demonstrate a scaffold architecture that combines interconnected porosity for cellular infiltration with sufficient filament continuity for mechanical support [64,65]. The distributions of pore volume, surface area, sphericity, and strand diameter further confirm that the scaffold possesses a consistent and well-defined microstructure without excessive irregularities or void collapse. It should be noted that the measurements reflect the lyophilized state, and absolute pore dimensions may shift upon rehydration; however, the relative spatial organization is preserved, validating nano-CT as an appropriate and reliable method for assessing the 3D architecture of such soft hydrogel scaffolds.

3.3. Material biocompatibility results

The cells were tested with all the materials for their proliferation during 48 h using the Resazurin reduction assay. Fig. 7 shows the relative metabolic activity of HSF cells after 48 h of culturing on different materials compared to PCL control. PCL scaffolds were used as a control because PCL is one of the most extensively studied synthetic polymers for tissue engineering and cell culture. Its cytocompatibility, slow degradation, and reproducibility are well documented in a broad

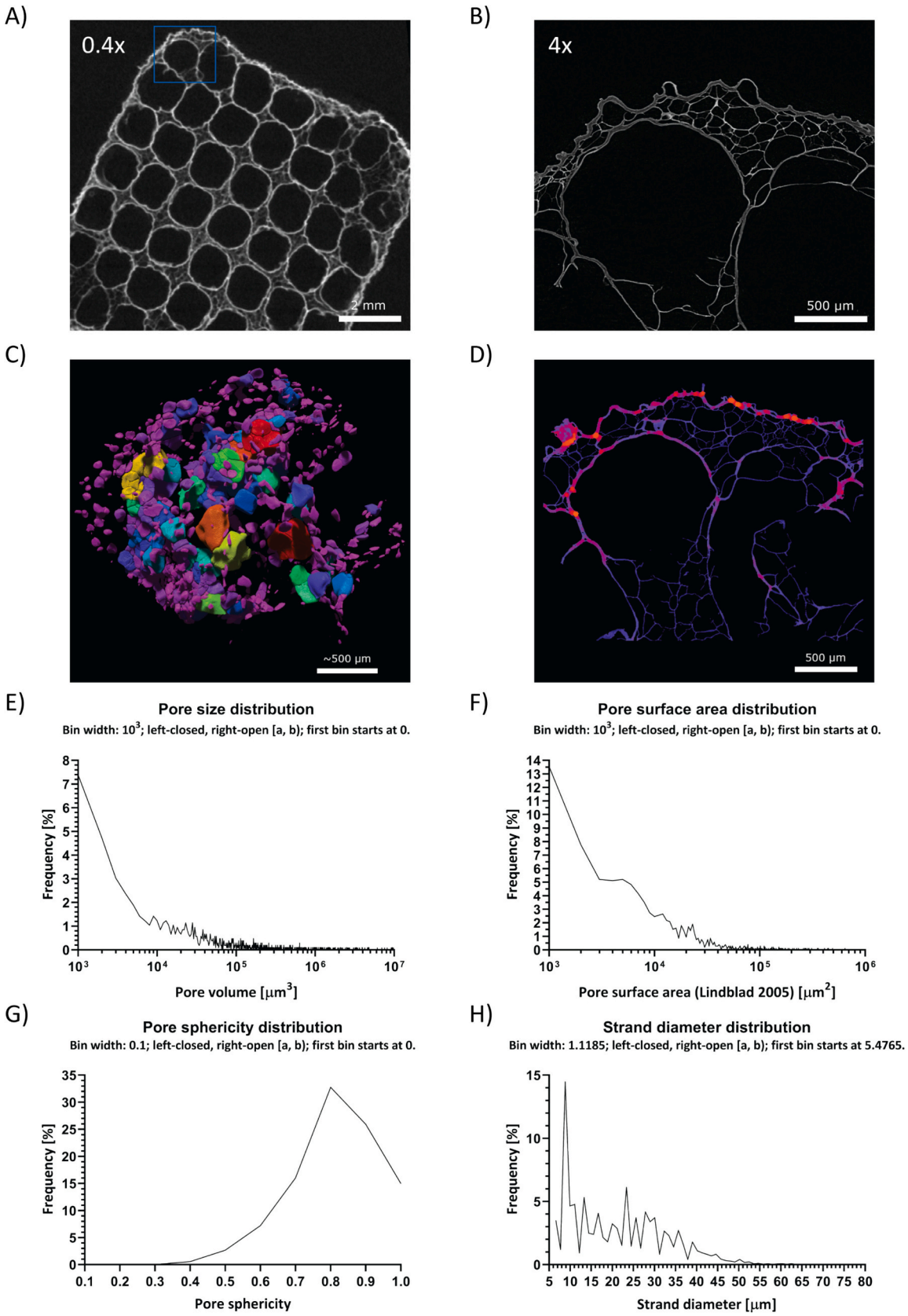

Fig. 6. Nano-CT morphology of lyophilized scaffolds. **A)** Low- and **B)** high-magnification cross-sections showing the pore network (scale bars 2 mm and 500 µm). **C)** Segmented pore objects and **D)** skeletonized strand network used for morphometry (scale bars 500 µm; note scale bar in panel C represents approximately 500 µm, as precise figure cannot be determined due to the 3D nature of the image). Derived morphometric distributions of **E)** pore volume, **F)** pore surface area, **G)** pore sphericity, and **H)** strand diameter. | Imaging: Zeiss Xradia 620 Versa, segmentation and analysis in Dragonfly 3D World. See Supplementary Information for full numerical values.

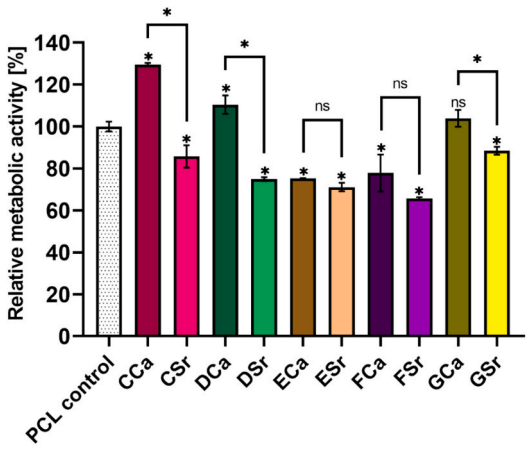

Fig. 7. Relative metabolic activity after 48 h of culture, measured by resazurin reduction assay, normalized to PCL scaffolds (set as 100 %). PCL was selected as a well-studied 3D-printed control material. Bars represent mean ± SD ($n = 3$ scaffolds per condition). Statistical significance was determined by one-way ANOVA with Bonferroni post-hoc; $p < 0.05$. The significant/not significant difference between pairs is denoted by asterisk/"ns" above the respective pair. The asterisk/"ns" just above the columns denotes the significant/not significant difference between the respective material and control.

range of applications [66–69]. What is more, the PCL surface of the scaffold has been proven to support the formation of stable functional EC monolayers [70]. Expertise with PCL has been consolidated within our laboratory through multiple projects, with recent publications demonstrating its robustness and reproducibility in fibroblast-based assays [56,71]. Importantly, PCL could be 3D printed into the exact same scaffold geometry as the hydrogel groups, which provided a reproducible 3D structural benchmark. While many studies still rely on 2D surfaces as controls, we considered it more rigorous to compare our hydrogel scaffolds against another 3D-printed material, thereby minimizing geometric and topographic differences.

Comparing the metabolic activity of the cells with those on PCL control, the cells on CCa, DCa, and GCa samples exhibited higher metabolic activity, while all others exhibited lower metabolic activity. Among Ca^{2+}-crosslinked scaffolds, CCa and DCa exceeded PCL – CCa: +29.5 percentage points (pp), 95 % CI 27.1–31.9, $P = 6.52 \times 10^{-7}$; DCa: +10.4 pp., 95 % CI 5.7–15.1, $P = 0.0107$, whereas ECa and FCa were lower (ECa: −24.8 pp., 95 % CI −27.2 to −22.4, $P = 1.27 \times 10^{-5}$; FCa: −22.2 pp., 95 % CI −31.4 to −13.0, $P = 0.0120$); GCa was comparable to PCL (+3.9 pp., 95 % CI −0.45 to 8.25, $P = 0.723$). All Sr^{2+}-crosslinked counterparts were below PCL, with the largest deficit for FSr: −34.3 pp. (95 % CI −36.7 to −31.9, $P = 7.10 \times 10^{-7}$); other decreases included CSr (−14.3 pp., 95 % CI −19.9 to −8.7, $P = 0.00564$), DSr (−25.1 pp., 95 % CI −27.5 to −22.7, $P = 1.09 \times 10^{-6}$), ESr (−28.9 pp., 95 % CI −31.7 to −26.1, $P = 6.66 \times 10^{-9}$), and GSr (−11.6 pp., 95 % CI −14.3 to −8.9, $P = 3.22 \times 10^{-5}$). Within each formulation, Ca^{2+}-crosslinked scaffolds showed higher metabolic activity than their Sr^{2+} counterparts (Ca—Sr mean differences +4.1 to +43.8 pp.; 95 % CIs entirely above 0), e.g., formulation C (CCa–CSr): +43.8 pp. (95 % CI 38.2–49.4; $P = 1.92 \times 10^{-5}$) and formulation E (ECa–ESr): +4.1 pp. (95 % CI 2.0–6.2; $P = 0.0195$). Comparing C vs D (both 5 % CMC but 3 % vs 5 % ALG) shows that higher ALG content reduces metabolic activity for both crosslinkers, consistent with Bohari et al. [72]; similarly, at 7 % CMC (E 1 % ALG vs F 3 % ALG), a reduction was evident for Sr^{2+} but not for Ca^{2+}. Increasing CMC from 5 % (C) to 7 % (F) at fixed 3 % ALG further decreased activity (both crosslinkers). Finally, adding 1.5 % NFC (comparing D vs G) increased activity for Sr^{2+}-crosslinked scaffolds, whereas for Ca^{2+} the difference was not significant (both DCa and GCa were numerically ≥ PCL, with DCa significantly above and GCa comparable to PCL).

The materials with the best results from previous tests were used for subsequent tests, which included cells; CCa, DCa, GCa, and GSr were selected for the next phase.

Live/Dead assay after 3 days of culture showed remarkable consistency in the results of all samples tested, indicating a uniform and comparable cell viability profile between different samples (shown in Fig. 8). A few dead cells are visible on all images of GCa sample image, the green signal prevails. The similarity of the results indicates the suitability and potential of all the formulations for applications requiring sustained cell viability. The results also provide a solid basis for further investigations and highlight their potential as promising candidates for tissue engineering.

3.4. Morphology assessment with cytoskeleton staining

Morphology of the cells on respective materials was observed. As can be seen from Fig. 9, the cells have a more elongated morphology on materials GCa and GSr showing that they adhere better and they adapt to the surface of the scaffold, as has also been observed in previous studies [73–75].

3.5. Functional cell properties in contact with the formulations

In the scope of functional cell testing, we have initially evaluated how different scaffold materials influence the cell phenotype over 30 days. The cells were exposed to a different set of materials, as in the previous tests.

For phenotype retention testing, 4 materials were used – the ones that proved most suitable in previous experiments – CCa, DCa, GCa, and GSr. It must be noted that the cell density inside the bioink was not very high, which resulted in not many cells being in the field of view (in a respective z-plane) at the same time. However, this was enough to confirm the retention of phenotype. Fig. 10 shows the images of all the markers in the first and last timepoints (0 days and 30 days).

The staining of both specific skin fibroblast markers (TE-7 and FSP-1), as well as the mesenchymal cell-specific filament vimentin, produced similar results across all timepoints in all bioink materials, which indicates phenotype retention on all selected materials. Of note, for reason unknown, DAPI did not stain very well on the TE-7 samples, so we included the images without including the DAPI layer.

TE-7's function is currently still unknown, but it is a specific antigen found in fibroblasts [76] and is used to assess HSF phenotype retention in this study. FSP-1, on the other hand, is an important marker of fibroblasts, that distincts them from αSMA-expressing myofibroblast subtype and is shown to be pro-angiogenic, balancing vascularization in favour of fibrosis [77], as it triggers angiogenic effects in human umbilical vein endothelial cells (HUVEC) [78], and synergises with VEGF as it enhances VEGFR-2 expression [79]. Vimentin endows fibroblasts with the contractile strength to remodel collagen into aligned parallel fibers which act as physical guides for endothelial cells to follow [80]. Loss of vimentin has also been shown to lower Notch signaling strength in endothelial cells, leading to poor mural cell recruitment and fragile, leaky capillaries [81]. What is more, van Beijnum et al. showed that extracellular vimentin is pro-angiogenic and functionally mimics VEGF action [82].

Next, structural and functional protein production was measured. Images of HSF monolayer culture ICC are presented in Fig. 11A below. This was performed to confirm that the cells indeed produce essential proteins for their function.

Collagens I and III are essential fibrillar collagens with distinct roles in tissue function. Collagen I, predominant in skin and bone, provides tensile strength and structural integrity [83–85], while collagen III, enriched in embryonic tissues, wound healing, and blood vessels, contributes to flexibility and vascular integrity [86,87]. Their production by HSF on the tested materials indicates good suitability for tissue models.

For control, the scaffolds were analyzed for autofluorescence – the results are shown in Fig. 11B.

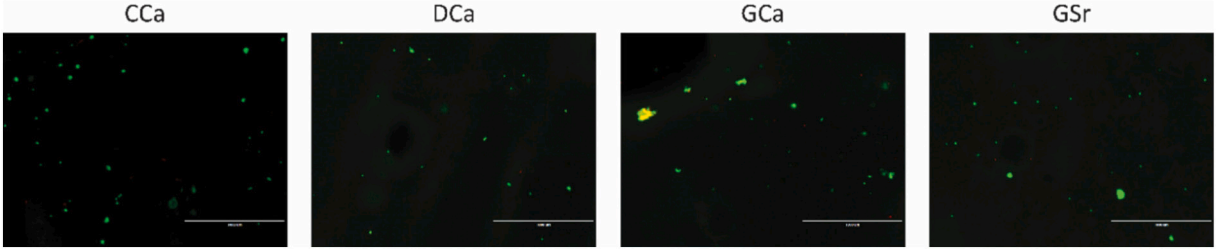

Fig. 8. Live/Dead assay of fibroblasts after 3 days of culture in selected scaffolds. Representative fluorescence images of CCa, DCa, GCa, and GSr scaffolds are shown. Green fluorescence (calcein-AM) indicates viable cells; red fluorescence (ethidium homodimer III) marks dead cells. Staining was performed according to the manufacturer's instructions (Biotium). Images were acquired using an EVOS FL Cell Imaging System at 4× magnification. Scale bar represents 1000 μm. (For interpretation of the references to colour in this figure legend, the reader is referred to the web version of this article.)

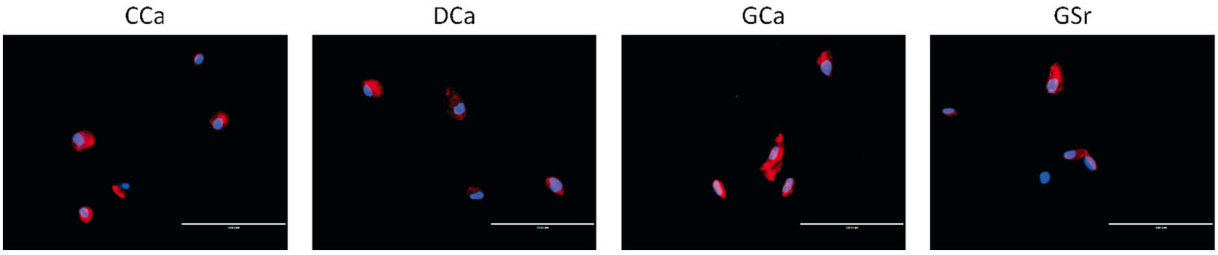

Fig. 9. Fibroblast morphology on CCa, DCa, GCa and GSr scaffolds after 3 days of culture. Cells were fixed in 4 % paraformaldehyde and stained with Alexa Fluor 555 Phalloidin (F-actin, red) and DAPI (nuclei, blue). Images were acquired with the EVOS FL Cell Imaging System at 40× magnification. Scale bar = 100 μm. (For interpretation of the references to colour in this figure legend, the reader is referred to the web version of this article.)

Similarly to the previous section, Fig. 12 shows images of the structural proteins in the first and last timepoints (0 days and 30 days).

It can be observed from Fig. 12A that the production of collagen I increased over time on all scaffolds, as the intensity of the green dye is greater after 30 days. Furthermore, in the case of the GSr sample, the protein production is already high at the beginning (0 days).

A similar pattern of increased expression of collagen III on all scaffold materials can be observed in Fig. 12C. A significant difference can be seen between the beginning and after 30 days, which indicates an increase in collagen III production. There is also a noticeable difference between the materials on day 0, where the green colour intensity is higher in the GCa sample.

On the other hand, the expression of fibronectin protein did not increase over time but is present in the cells on all scaffold materials, which can be seen in Fig. 12E. The presence of fibronectin plays a role in organizing and stabilizing collagen fibers in the ECM, as it interacts with collagen and helps in the assembly and alignment of collagen fibrils, contributing to the structural integrity of the skin [88,89].

Quantitative image analysis confirmed trends observed in the micrographs. Collagen I intensity (Fig. 12B) increased significantly from day 0 to day 30 in all scaffold groups except GSr, with the CCa formulation showing the largest relative increase (approximately 33-fold). Collagen III intensity (Fig. 12D) increased over 30 days in all scaffold groups, and GCa and GSr exhibited comparatively higher collagen III at the first timepoint. In contrast, fibronectin intensity (Fig. 12F) did not change so drastically between day 0 and day 30 across any of the groups, except for CCa, where it increased approximately 5-fold. Measurements were performed on identical ROIs and expressed as mean gray value, mean ± SD, with $n = 2$ biological replicates and five fields per scaffold.

Finally, cell function was evaluated by the release of specific molecular markers using ELISA. FGF-2 and VEGF production were evaluated to determine which material formulations positively or negatively influence the production and release of these factors.

It has been studied that FGF-2 and VEGF, both of which have very important roles in angiogenesis, are produced by fibroblasts [20,90–95]. We wanted to evaluate the influence of the scaffold material on growth factor production. The results of ELISA assays of growth factor concentrations in cell culture media from wells with cells embedded in different scaffold materials are presented in Fig. 13A **and** Fig. 13B below.

At day 3, CCa showed the highest secretion (738.1 pg ml^{-1}, 95 % CI 720.0–756.2) followed by DCa (630.8, 95 % CI 620.6–641.0); both were higher than other hydrogels ($P < 0.05$ for the main pairwise contrasts between materials). By day 30, CCa remained higher than DCa (456.2 vs 340.1 pg ml^{-1}; 95 % CI 446.0–466.4 vs 337.1–343.1; $P < 0.01$), GCa (339.4; 95 % CI 326.8–351.9; $P < 0.01$), and GSr (295.0; 95 % CI 285.0–304.9; $P < 0.01$). Across hydrogels, VEGF secretion was modest and broadly similar. At day 3, no pairwise differences reached significance (e.g., CCa 48.0 [95 % CI 32.9–63.0] vs DCa 32.8 [95 % CI 27.1–38.5]; $P = 0.154$). At day 7, differences again were insignificant (e.g., DCa 56.9 [95 % CI 32.3–81.5] vs GCa 54.3 [95 % CI 33.8–74.8]; $P = 0.312$). By day 30, VEGF levels converged at low values across all hydrogels (~11.8–13.9 pg ml^{-1}), with no significant pairwise differences (all $P > 0.05$). Overall, FGF-2 exhibited early peaks in CCa/DCa at day 3, with CCa remaining elevated at day 30, whereas VEGF stayed uniformly low without material-dependent separation. These secretion patterns parallel the Alamar Blue results (higher metabolic activity for Ca^{2+} vs Sr^{2+} within formulations) and support that scaffold composition and crosslinking modulate fibroblast pro-angiogenic signaling. While functional angiogenesis assays were not performed here, CCa showed the most favorable growth-factor profile among the hydrogels tested.

To conclude, all materials support phenotype retention, structural protein production, and cell functionality over 30 days. Furthermore, our results also suggest that by modulating the scaffold material and crosslinking agent, a control over growth factor production can be achieved.

Beyond confirming viability and phenotype retention, the results point to specific stromal functions of fibroblasts within engineered scaffolds. Collagen I and III deposition provides a fibrillar framework that not only increases mechanical competence but also serves as a structural guide for endothelial cell alignment and migration [96,97]. Fibronectin, observed across all scaffolds, likely stabilizes collagen

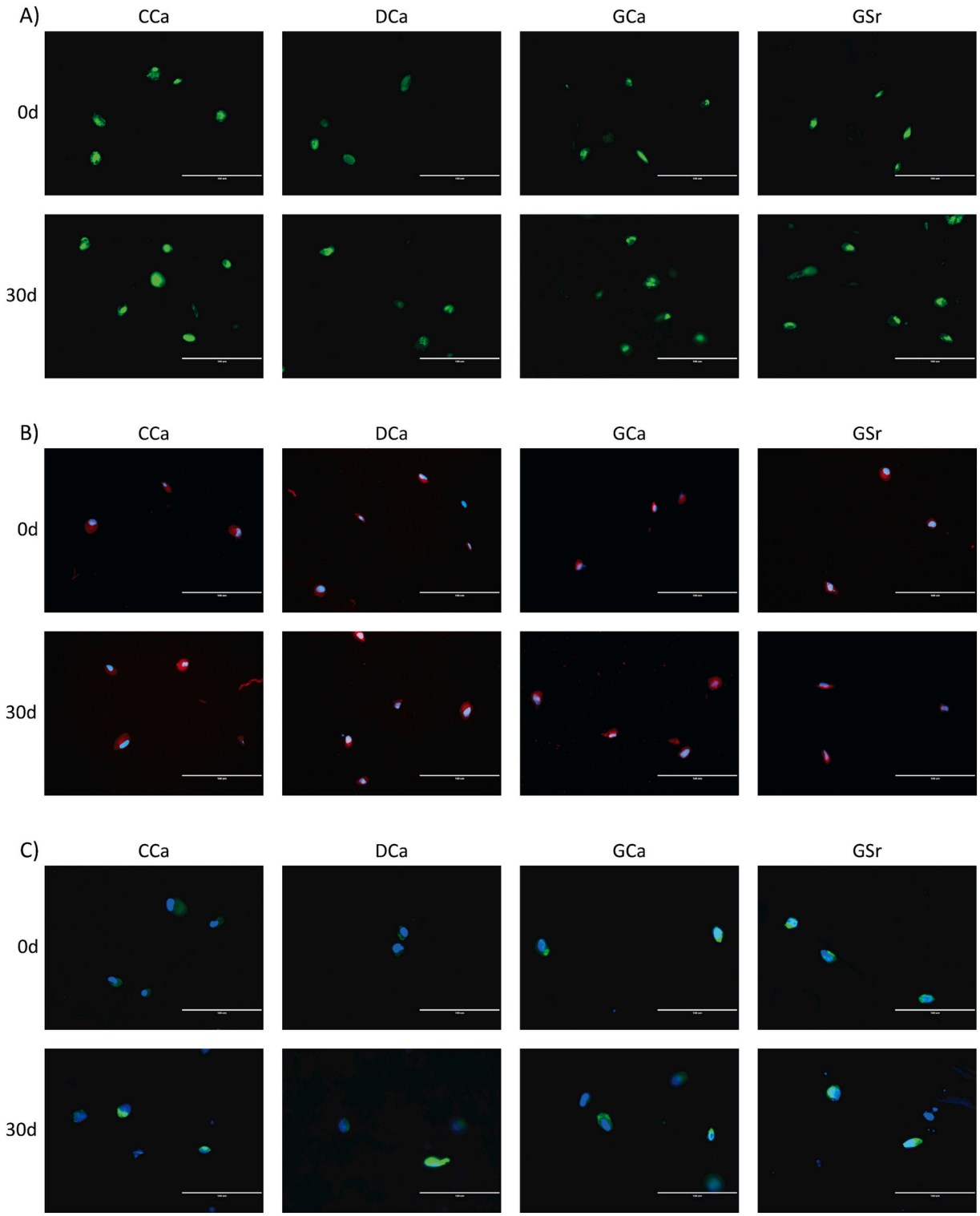

Fig. 10. Phenotype retention in fibroblast-laden scaffolds at day 0 and day 30. **A)** TE-7 (green), **B)** FSP-1 (red), and **C)** Vimentin (green) staining. Counterstained with DAPI staining of nuclei (blue). | Cells were cultured in ADMEM +5 % FBS at 37 °C and 5 % CO_2, with medium changed every 3–4 days. Scaffolds were fixed, cryosectioned at 50 μm, and stained with primary and conjugated secondary antibodies as described in Methods. Images were acquired using EVOS FL Cell Imaging System at 40× magnification. Scale bar represents 100 μm. (For interpretation of the references to colour in this figure legend, the reader is referred to the web version of this article.)

fibrils and facilitates matrix remodeling, consistent with its role in vascular sprouting [98–100]. The secretion of VEGF and FGF-2 further highlights the paracrine potential of fibroblasts in shaping the vascular niche. While VEGF is a key angiogenic initiator, its excess can lead to immature, leaky vessels, underscoring the importance of balanced secretion. In contrast, FGF-2 has been shown to promote more mature vascularization by stimulating endothelial sprouting and mural cell recruitment [101]. Together, these findings illustrate how scaffold composition modulates fibroblast-derived cues that may influence angiogenesis in co-culture or in vivo contexts.

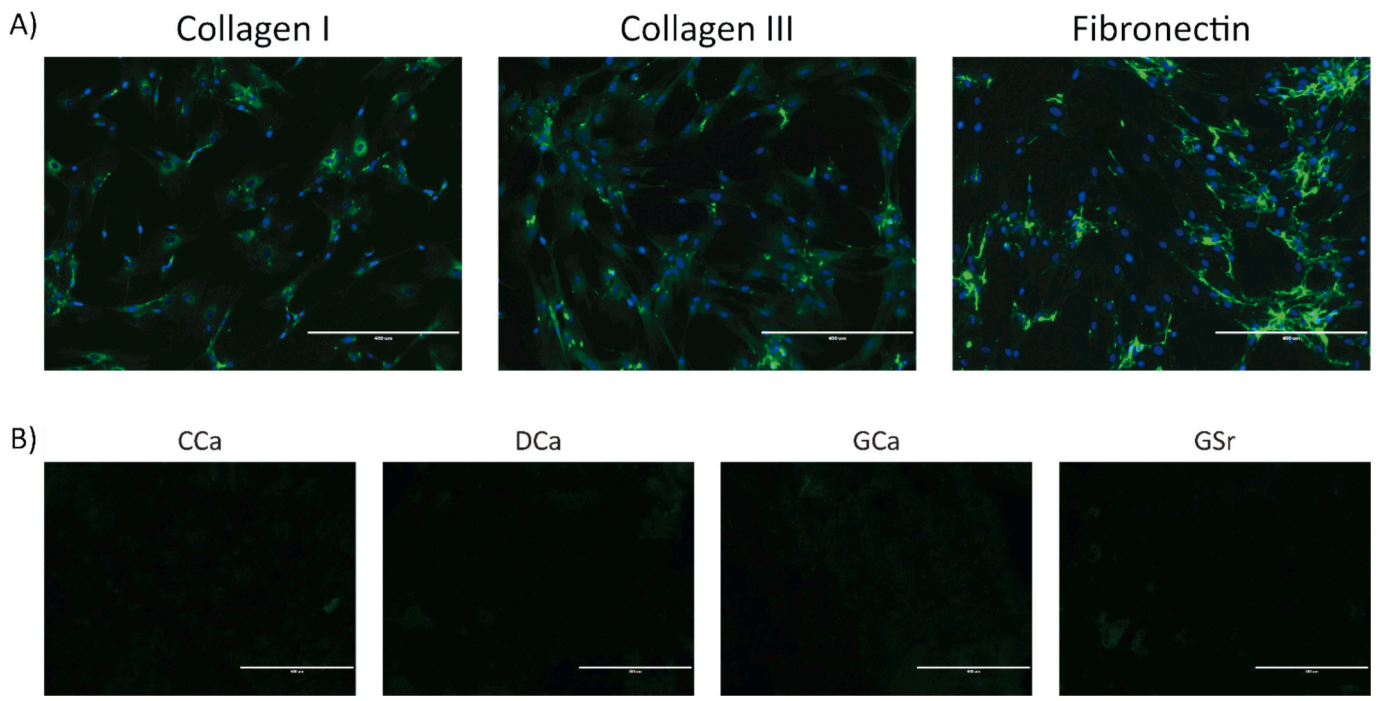

Fig. 11. A) Staining of structural and functional proteins on HSF monolayer. Structural proteins – Collagen I (ab138492, 1:2000 + ab150077, 1:200), Collagen III (nb600–594, 1:100 + ab150077, 1:200), and Fibronectin (ab198933, 1:100). ECM proteins are shown in green; nuclei counterstained with DAPI (blue). **B)** Autofluorescence analysis of the scaffolds. The results show that the scaffolds exhibited virtually no autofluorescence. The parameters of the microscope were the same as for subsequent analysis. | Images acquired at 10× magnification. Scale bar represents 400 μm. (For interpretation of the references to colour in this figure legend, the reader is referred to the web version of this article.)

A notable strength of this study is the direct comparison of Ca^{2+}- and Sr^{2+}-crosslinked scaffolds under identical conditions. The systematic comparison of Ca^{2+} versus Sr^{2+} crosslinking demonstrates that ion selection is not a trivial choice: it alters long-term mechanics and fibroblast activity, providing a tunable parameter for rational bioink design. These observations are consistent with evidence that ECM stiffness and composition regulate endothelial-pericyte interactions and vessel maturation [102]. Another strength of this study is the extended 30-day culture period. Most fibroblast-laden hydrogel investigations are limited to one or two weeks, which may overlook later changes in matrix deposition and growth factor secretion. By following the constructs for 30 days, we captured long-term trends in fibroblast activity, which are particularly relevant for applications requiring sustained tissue support. This work also stands out for its multiparametric approach. By combining rheological analysis, degradation studies, mechanical testing, cell viability assays, immunofluorescence, and growth factor quantification, we assessed fibroblast–scaffold interactions from multiple angles. This comprehensive dataset provides a more reliable basis for identifying design considerations than single-parameter investigations.

3.6. Limitations and future outlook

While our findings demonstrate that fibroblast-laden alginate/cellulose scaffolds support long-term viability, ECM deposition, and secretion of angiogenic growth factors, important limitations should be noted.

The study does not include co-cultures with endothelial or other vascular cells coupled with functional angiogenesis assays or in vivo validation. Instead, angiogenic relevance was inferred indirectly from fibroblast-derived ECM production and secretion of VEGF and FGF-2.

While out of scope, these additional approaches would provide a more direct demonstration of angiogenesis and physiologically relevant neovascularization and its connection to paracrine signaling. Here, the primary focus was setting a baseline for properties that are necessary before advancing to more complex multicellular or in vivo models by demonstrating sustained fibroblast viability, phenotype, ECM deposition, and growth factor secretion.

ECM analysis was based on semi-quantitative immunofluorescence. Complementary biochemical assays or proteomics would provide more comprehensive information on ECM composition and remodeling.

Viscosity of the precursor gels was assessed under steady shear, as this parameter directly governs extrusion behavior and 3D printing fidelity. Oscillatory measurements of storage (G') and loss (G'') moduli were not performed. While such data would provide additional insights into the relative elastic and viscous contributions, they were not essential for the scope of this work. After ionic crosslinking, the viscoelastic properties of the materials change abruptly, and oscillatory values of the precursor state would not reflect the final scaffold mechanics. Future studies that focus on long-term rheological stability of crosslinked constructs may incorporate small-amplitude oscillatory shear testing to complement the present viscosity-based analysis. Additionally, we did not quantify crosslinking density, bound cation content, or ion-exchange kinetics; therefore, mechanistic attributions regarding Ca^{2+} vs. Sr^{2+} should be interpreted cautiously and as consistent with prior literature rather than demonstrated directly here.

While PCL offered a stable, well-studied, and geometrically comparable control, it does not share the viscoelastic properties of hydrogels. Therefore, the biological differences observed between the hydrogel and PCL groups should not be interpreted solely as material-driven but also as reflecting distinct mechanical and biochemical environments. A hydrogel-based control would provide a more directly comparable baseline and is planned for future work.

Features smaller than the imaging voxel (2.7382 μm) were not resolved by nano-CT, and therefore, nanoscale surface roughness and fibrillar details are not captured.

Future studies should address these aspects to broaden the translational relevance of the findings.

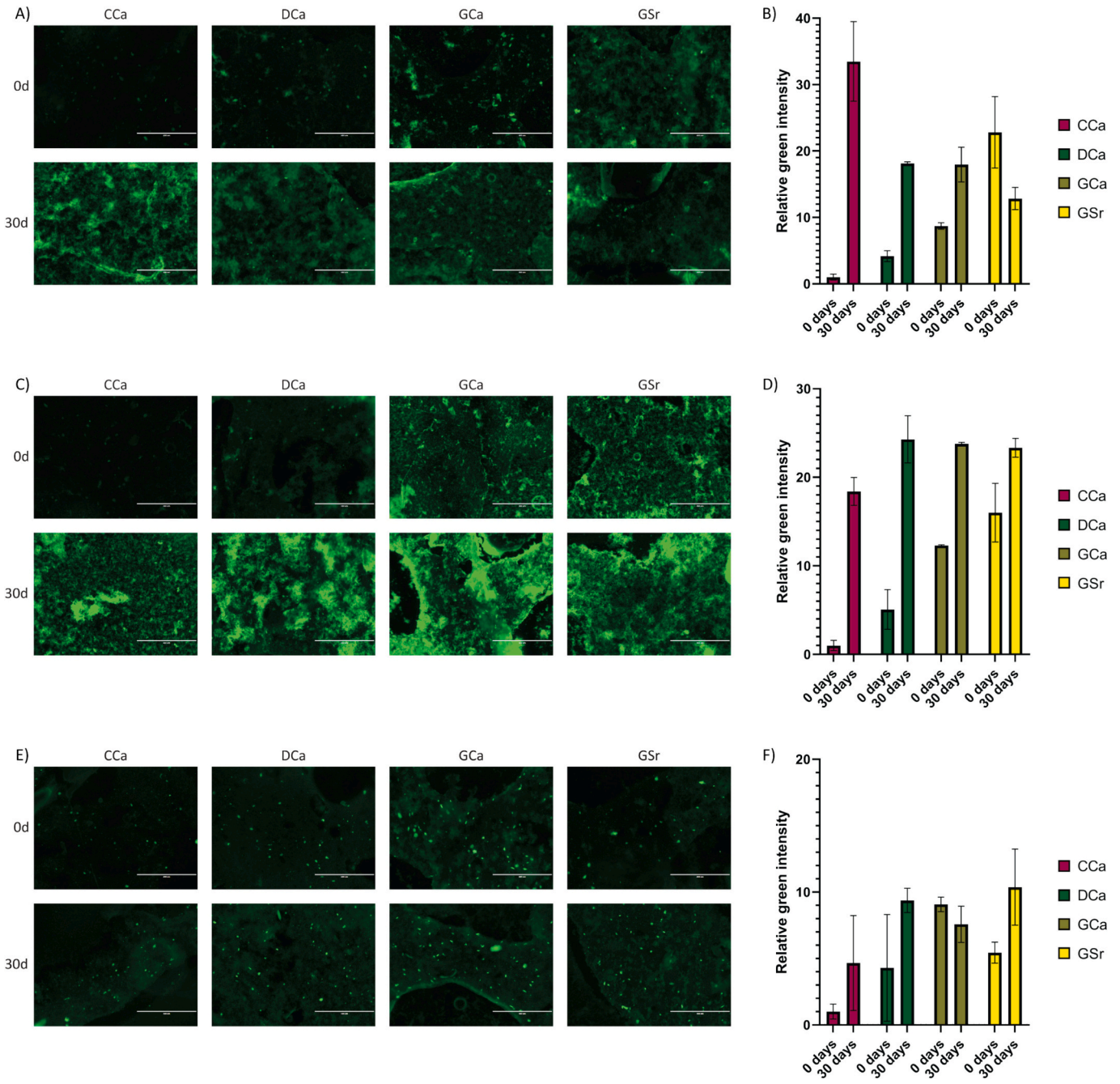

Fig. 12. Immunofluorescence staining of fibroblast ECM proteins at day 0 and day 30, and quantitative analysis of fluorescence intensities. **(A)** Collagen I (ab138492, 1:2000 + ab150077, 1:200), **(B)** Quantitative analysis of collagen I fluorescence analysis, **(C)** Collagen III (nb600–594, 1:100 + ab150077, 1:200), **(D)** Quantitative analysis of collagen III fluorescence analysis, **(E)** Fibronectin (ab198933, 1:100), **(F)** Quantitative analysis of fibronectin fluorescence analysis. | ECM proteins are shown in green. Cells were cultured for up to 30 days in ADMEM +5 % FBS at 37 °C and 5 % CO_2, with medium refreshed every 3–4 days. Scaffolds were fixed, cryosectioned at 50 μm, and stained according to manufacturer protocols. Images were acquired at 10× magnification with the EVOS FL Cell Imaging System. Scale bar represents 400 μm. Bars on the graphs show mean ± SD ($n = 2$ biological replicates, five fields per scaffold); values are mean gray value (a.u.), normalized to the lowest value of the group set to 1.000. (For interpretation of the references to colour in this figure legend, the reader is referred to the web version of this article.)

4. Conclusions

This study systematically compared seven 3D-printed hydrogel formulations composed of sodium alginate and carboxymethyl cellulose (including one with nanofibrillated cellulose) to optimize fibroblast-laden scaffolds that preserve fibroblast phenotype and promote robust ECM and growth-factor secretion. The samples, crosslinked with either calcium chloride or strontium chloride, were evaluated for rheological properties, degradability, mechanical stiffness, followed by several analyses using human skin fibroblasts (e.g., biocompatibility assays, phenotype preservation over time and the capability of cells to perform their desired function) over 30 days. The rationale behind the 30-day duration of the experiments is the need for sustained fibroblast activity, as continuous ECM production and growth-factor expression are required to support the gradual development of stable microvasculature [103,104].

Formulations with higher CMC content exhibited higher viscosity than formulations with higher ALG content. A comparison of

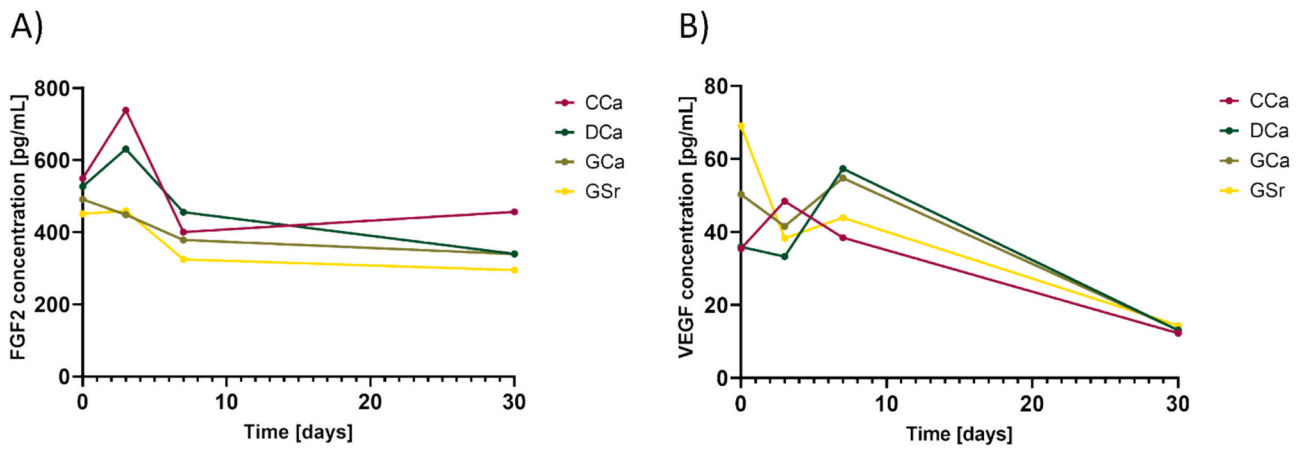

Fig. 13. Growth factor secretion measured by ELISA. **A)** FGF-2 (ab99979) and **B)** VEGF (ab222510) concentrations in cell culture media from wells with cells embedded in different scaffold materials, at 0, 3, 7, and 30 days. | Bioink scaffolds (CCa, DCa, GCa, GSr) were seeded with human skin fibroblasts and cultured in ADMEM +5 % FBS at 37 °C and 5 % CO_2. Medium was replaced 72 h before each sampling. Samples collected at 0, 3, 7, and 30 days were frozen at −20 °C and assayed in parallel.

formulations D and G (same amount of ALG and CMC) also shows that the addition of NFC significantly increased the viscosity of the hydrogel. The viscosity control is important in tissue-engineering, as it translates into scaffolds with ECM-like stiffness and porosity that shield cells from excessive shear, support high post-print viability, and provide mechanical cues that steer the cells toward different phenotypes – results already demonstrated in NFC–alginate constructs both in vitro and in vivo [105,106]. All materials performed similarly in degradation tests and did not deteriorate significantly after being suspended in cell culture media for three weeks. Under cell culture conditions, all scaffolds showed comparable degradation tendencies and maintained their weight for up to 21 days. Regarding the mechanical properties of the scaffold, the apparent compressive modulus of the samples remained constant up to approx. 45 % strain, providing stable mechanobiological cue for resident cells, making the biochemical responses (adhesion, spreading, lineage commitment) predictable and homogeneous across the graft – a major design goal in mechanobiology [107]. With an increased submersion duration, the apparent compressive modulus decreased steadily. The stress reached a plateau for some samples after 1 day and started increasing sharply at around 60 % strain. $CaCl_2$-crosslinked samples showed an initial decrease but stabilized, while the apparent compressive modulus of $SrCl_2$-crosslinked samples decreased continuously. $SrCl_2$-crosslinked samples retained a significantly higher apparent compressive modulus than $CaCl_2$-crosslinked samples. NFC-incorporated specimens stabilized after 3 days without a further decrease in apparent compressive modulus. These results suggest that by modulating scaffold material and crosslinking agents a control over rheological and mechanical properties of scaffolds can be achieved. Moreover, the Live/Dead assay did not show cytotoxicity in any of the samples. However, the $CaCl_2$-crosslinked samples showed higher cell viability, while increasing CMC (from 5 % to 7 %) decreased viability (groups C and F). The addition of NFC slightly decreased viability, but viability was higher than that of the control group, nevertheless which confirms the suitability of various formulations, meeting different tissue engineering goals. The production of collagen I and III proteins increased over time, while fibronectin expression remained constant. After 30 days, the concentrations of growth factors (FGF-2 and VEGF) were similar, except within CCa sample, which had a significantly higher FGF-2 content, promising enhanced growth factor secretion in this sample, which may be consistent with pro-angiogenic potential. The FGF-2 levels peaked in CCa and DCa on day 3 and remained higher than in GCa and GSr. VEGF levels peaked in CCa on day 3 but decreased significantly after 3 days. The ELISA results correlated with those of the Alamar Blue assay. In conclusion, all materials supported phenotype retention and structural protein production, but only CCA boosted specific microvasculature-promoting cell functionality of skin fibroblasts over 30 days. Our results also suggest that by modulating scaffold material and crosslinking, fibroblast-mediated VEGF and FGF-2 release can be adjusted. While these findings provide useful design considerations, they are exploratory and based on a single fibroblast line; further studies are needed to confirm their generality.

In summary, fibroblast-laden ALG-CMC scaffolds supported cell viability and phenotype maintenance over 30 days of culture. Fibroblasts deposited ECM proteins, including collagen I, collagen III, and fibronectin, and secreted the growth factors VEGF and FGF-2. These outcomes demonstrate that the scaffolds provide a supportive in vitro environment for fibroblast function. While the extent of response varied among formulations, with CCa scaffolds (Ca^{2+}-crosslinked 3 %ALG-5 % CMC formulation) showing particularly favorable outcomes, all groups maintained basic fibroblast activity. These results establish a basis for identifying design considerations in bioink development, although direct angiogenic activity was not tested in this study.

A key strength of this work is the systematic, long-term comparison of Ca^{2+}- and Sr^{2+}-crosslinked ALG-CMC scaffolds, which provides insight into how crosslinking affects mechanical properties, fibroblast viability and phenotype, ECM deposition, and angiogenic growth factor secretion. The 30-day follow-up is a distinctive feature of this study and provides important information on how scaffold composition influences fibroblast function over prolonged culture periods. Taken together, the multiparametric evaluation of scaffold properties and fibroblast function adds robustness to the findings and enhances their relevance for future bioink development.

CRediT authorship contribution statement

Jernej Vajda: Writing – original draft, Visualization, Validation, Resources, Project administration, Methodology, Investigation, Funding acquisition, Formal analysis, Data curation, Conceptualization. **Dragana Bjelić:** Writing – original draft. **Boštjan Vihar:** Writing – review & editing, Validation, Supervision, Resources, Project administration, Methodology, Funding acquisition, Conceptualization. **Matej Vesenjak:** Writing – original draft, Resources. **Polona Dobnik Dubrovski:** Investigation. **Lidija Gradišnik:** Investigation. **Monika Belak:** Writing – original draft. **Uroš Maver:** Writing – review & editing, Supervision, Resources, Project administration, Methodology, Funding acquisition, Conceptualization. **Marko Milojević:** Writing – review & editing, Visualization, Funding acquisition, Formal analysis, Data curation.

Declaration of competing interest

All authors declare no financial or non-financial competing interests.

Acknowledgements

The authors would like to acknowledge the financial support from the Slovenian Research and Innovation Agency – ARIS (grant numbers: N1-0305, L7-4494, J3-4524, J3-50098, J7-60120, P3-0036, I0-0029, and through the Young Researcher Program), as well as from the New Harvest foundation and the European Commission for funding through FEASTS (Project ID 101136749, call HORIZON-CL6-2023-FARM2FORK-01-13).

Appendix A. Supplementary data

Supplementary data to this article can be found online at https://doi.org/10.1016/j.ijbiomac.2025.148701.

Data availability

Data is shared as supplementary information.

References

[1] R. Langer, J. Vacanti, Advances in tissue engineering, J. Pediatr. Surg. 51 (1) (2016) 8–12.
[2] T.A. Ahmed, E.V. Dare, M. Hincke, Fibrin: a versatile scaffold for tissue engineering applications, Tissue Eng. Part B Rev. 14 (2) (2008) 199–215.
[3] R. Parenteau-Bareil, R. Gauvin, F. Berthod, Collagen-Based Biomaterials for Tissue Engineering Applications, Materials 3 (3) (2010) 1863–1887.
[4] O. Aarstad, E.B. Heggset, I.S. Pedersen, S.H. Bjørnøy, K. Syverud, B.L. Strand, Mechanical properties of composite hydrogels of alginate and cellulose nanofibrils, Polymers (Basel) 9 (8) (2017).
[5] D.R. Sahoo, T. Biswal, Alginate and its application to tissue engineering, SN Applied Sciences 3 (1) (2021) 30.
[6] J. Sun, H. Tan, Alginate-Based Biomaterials for Regenerative Medicine Applications, Materials (Basel) 6 (4) (2013) 1285–1309.
[7] F. Baino, G. Novajra, C. Vitale-Brovarone, Bioceramics and Scaffolds: A Winning Combination for Tissue Engineering, Front. Bioeng. Biotechnol. 3 (2015).
[8] M.T. Frassica, M.A. Grunlan, Perspectives on Synthetic Materials to Guide Tissue Regeneration for Osteochondral Defect Repair, ACS Biomater Sci. Eng. 6 (8) (2020) 4324–4336.
[9] D.S. Kohane, R. Langer, Polymeric Biomaterials in Tissue Engineering, Pediatr. Res. 63 (5) (2008) 487–491.
[10] J.-N. Fu, X. Wang, M. Yang, Y.-R. Chen, J.-Y. Zhang, R.-H. Deng, Z.-N. Zhang, J.-K. Yu, F.-Z. Yuan, Scaffold-Based Tissue Engineering Strategies for Osteochondral Repair, Front. Bioeng. Biotechnol. 9 (2022).
[11] R. Langer, J.P. Vacanti, Tissue Engineering, Science 260 (5110) (1993) 920–926.
[12] A.J. Engler, S. Sen, H.L. Sweeney, D.E. Discher, Matrix elasticity directs stem cell lineage specification, Cell 126 (4) (2006) 677–689.
[13] J.H. Jang, L.D. Shea, Controllable delivery of non-viral DNA from porous scaffolds, J. Control. Release 86 (1) (2003) 157–168.
[14] J. Vajda, M. Milojević, U. Maver, B. Vihar, Microvascular tissue engineering—a review, Biomedicines 9 (6) (2021) 589.
[15] J. Tien, Tissue Engineering of the Microvasculature, 2019, pp. 1155–1212.
[16] J.G. Nemeno-Guanzon, S. Lee, J.R. Berg, Y.H. Jo, J.E. Yeo, B.M. Nam, Y.-G. Koh, J.I. Lee, Trends in Tissue Engineering for Blood Vessels, J. Biomed. Biotechnol. 2012 (2012) 956345.
[17] L. Lamalice, F. Le Boeuf, J. Huot, Endothelial Cell Migration During Angiogenesis, Circ. Res. 100 (6) (2007) 782–794.
[18] C. Marziano, G. Genet, K.K. Hirschi, Vascular endothelial cell specification in health and disease, Angiogenesis 24 (2) (2021) 213–236.
[19] C.G.M. van Dijk, F.E. Nieuweboer, J.Y. Pei, Y.J. Xu, P. Burgisser, E. van Mulligen, H. el Azzouzi, D.J. Duncker, M.C. Verhaar, C. Cheng, The complex mural cell: Pericyte function in health and disease, Int. J. Cardiol. 190 (2015) 75–89.
[20] A.C. Newman, M.N. Nakatsu, W. Chou, P.D. Gershon, C.C. Hughes, The requirement for fibroblasts in angiogenesis: fibroblast-derived matrix proteins are essential for endothelial cell lumen formation, Mol. Biol. Cell 22 (20) (2011) 3791–3800.
[21] L.E. Tracy, R.A. Minasian, E.J. Caterson, Extracellular Matrix and Dermal Fibroblast Function in the Healing Wound, Adv Wound Care (New Rochelle) 5 (3) (2016) 119–136.
[22] M.J. Cross, L. Claesson-Welsh, FGF and VEGF function in angiogenesis: signalling pathways, biological responses and therapeutic inhibition, Trends Pharmacol. Sci. 22 (4) (2001) 201–207.
[23] G.E. Davis, W. Koh, A. Sacharidou, K.E. Fisher, Role of extracellular matrix in vascular morphogenesis, FASEB J. 21 (5) (2007) A82.
[24] G.E. Davis, D.R. Senger, Endothelial extracellular matrix: biosynthesis, remodeling, and functions during vascular morphogenesis and neovessel stabilization, Circ. Res. 97 (11) (2005) 1093–1107.
[25] P. Lu, K. Takai, V.M. Weaver, Z. Werb, Extracellular matrix degradation and remodeling in development and disease, Cold Spring Harb. Perspect. Biol. 3 (12) (2011).
[26] M. Kasravi, A. Ahmadi, A. Babajani, R. Mazloomnejad, M.R. Hatamnejad, S. Shariatzadeh, S. Bahrami, H. Niknejad, Immunogenicity of decellularized extracellular matrix scaffolds: a bottleneck in tissue engineering and regenerative medicine, Biomaterials Research 27 (1) (2023) 10.
[27] E. Rezvani Ghomi, N. Nourbakhsh, M. Akbari Kenari, M. Zare, S. Ramakrishna, Collagen-based biomaterials for biomedical applications, J. Biomed. Mater. Res. B Appl. Biomater. 109 (12) (2021) 1986–1999.
[28] B. Demirbag, P.Y. Huri, G.T. Kose, A. Buyuksungur, V. Hasirci, Advanced cell therapies with and without scaffolds, Biotechnol. J. 6 (12) (2011) 1437–1453.
[29] A.C. Duarte, E.C. Costa, H.A.L. Filipe, S.M. Saraiva, T. Jacinto, S.P. Miguel, M. P. Ribeiro, P. Coutinho, Animal-derived products in science and current alternatives, Biomaterials Advances 151 (2023) 213428.
[30] S. Campuzano, A.E. Pelling, Scaffolds for 3D Cell Culture and Cellular Agriculture Applications Derived From Non-animal Sources, Frontiers in Sustainable Food Systems 3 (2019).
[31] M. Jin, J. Shi, W. Zhu, H. Yao, D.-A. Wang, Polysaccharide-based biomaterials in tissue engineering: a review, Tissue Eng. Part B Rev. 27 (2020).
[32] H. Seddiqi, E. Oliaei, H. Honarkar, J. Jin, L.C. Geonzon, R.G. Bacabac, J. Klein-Nulend, Cellulose and its derivatives: towards biomedical applications, Cellulose 28 (4) (2021) 1893–1931.
[33] K. Petzold-Welcke, K. Römhild, S. Daus, T. Heinze, Xylan derivatives and their application potential – Mini-review of own results, Carbohydr. Polym. 100 (2014) 80–88.
[34] M. Witzler, A. Alzagameem, M. Bergs, B.E. Khaldi-Hansen, S.E. Klein, D. Hielscher, B. Kamm, J. Kreyenschmidt, E. Tobiasch, M. Schulze, Lignin-Derived Biomaterials for Drug Release and Tissue Engineering, Molecules 23 (8) (2018).
[35] J.C. Courtenay, R.I. Sharma, J.L. Scott, Recent advances in modified cellulose for tissue culture applications, Molecules 23 (3) (2018).
[36] T.H. Jovic, G. Kungwengwe, A.C. Mills, I.S. Whitaker, Plant-Derived Biomaterials: A Review of 3D Bioprinting and Biomedical Applications, Front Mech Eng 5 (2019).
[37] R. Ahmad Raus, W.M.F. Wan Nawawi, R.R. Nasaruddin, Alginate and alginate composites for biomedical applications, Asian J. Pharm. Sci. 16 (3) (2021) 280–306.
[38] S. Sedighim, Y. Chen, C. Xu, R. Mohindra, H. Liu, D.K. Agrawal, F.G. Thankam, Carboxymethyl cellulose–alginate interpenetrating hydroxy ethyl methacrylate crosslinked polyvinyl alcohol reinforced hybrid hydrogel templates with improved biological performance for cardiac tissue engineering, Biotechnol. Bioeng. 120 (3) (2023) 819–835.
[39] A. Kavand, F. Noverraz, S. Gerber-Lemaire, Recent Advances in Alginate-Based Hydrogels for Cell Transplantation Applications, Pharmaceutics 16 (4) (2024).
[40] G. Guagliano, C. Volpini, J. Camilletti, F. Donnaloja, F. Briatico-Vangosa, L. Visai, P. Petrini, Internally crosslinked alginate-based bioinks for the fabrication ofin vitrohepatic tissue models, Biofabrication 15 (3) (2023).
[41] H. Malektaj, A.D. Drozdov, J. deClaville Christiansen, Mechanical Properties of Alginate Hydrogels Cross-Linked with Multivalent Cations, Polymers (Basel) 15 (14) (2023).
[42] N. Grunberg, A. McMeeking, E. Dieckmann, C. Cheeseman, Development of printable bacterial nanocellulose bioinks for bioprinting applications, Biotechnology for Sustainable Materials 1 (1) (2024) 14.
[43] K.H. Lee, S.J. Shin, Y. Park, S.H. Lee, Synthesis of cell-laden alginate hollow fibers using microfluidic chips and microvascularized tissue-engineering applications, Small 5 (11) (2009) 1264–1268.
[44] A. Habib, V. Sathish, S. Mallik, B. Khoda, 3D printability of alginate-carboxymethyl cellulose hydrogel, Materials 11 (3) (2018) 454.
[45] V. Kanikireddy, K. Varaprasad, T. Jayaramudu, C. Karthikeyan, R. Sadiku, Carboxymethyl cellulose-based materials for infection control and wound healing: A review, Int. J. Biol. Macromol. 164 (2020) 963–975.
[46] A. Dufresne, Nanocellulose: a new ageless bionanomaterial, Mater. Today 16 (6) (2013) 220–227.
[47] D. Klemm, F. Kramer, S. Moritz, T. Lindström, M. Ankerfors, D. Gray, A. Dorris, Nanocelluloses: A New Family of Nature-Based Materials, Angew. Chem. Int. Ed. 50 (24) (2011) 5438–5466.
[48] Y. Wang, Z. Shen, H. Wang, Z. Song, D. Yu, G. Li, X. Liu, W. Liu, Progress in research on metal ion crosslinking alginate-based gels, Gels 11 (1) (2025) 16.
[49] Y. Liu, L. Li, X. Li, H. Cherif, S. Jiang, F. Ghezelbash, M.H. Weber, D. Juncker, N. Y.K. Li-Jessen, L. Haglund, J. Li, Viscoelastic hydrogels regulate adipose-derived mesenchymal stem cells for nucleus pulposus regeneration, Acta Biomater. 180 (2024) 244–261.
[50] L. Bacakova, J. Pajorova, M. Bacakova, A. Skogberg, P. Kallio, K. Kolarova, V. Svorcik, Versatile Application of Nanocellulose: From Industry to Skin Tissue Engineering and Wound Healing, Nanomaterials 9 (2) (2019) 164.
[51] H. Luo, R. Cha, J. Li, W. Hao, Y. Zhang, F. Zhou, Advances in tissue engineering of nanocellulose-based scaffolds: A review, Carbohydr. Polym. 224 (2019) 115144.
[52] M.C. García, M.C. Alfaro, N. Calero, J. Muñoz, Influence of polysaccharides on the rheology and stabilization of α-pinene emulsions, Carbohydr. Polym. 105 (2014) 177–183.
[53] M. Milojević, L. Gradišnik, J. Stergar, M. Skelin Klemen, A. Stožer, M. Vesenjak, P. Dobnik Dubrovski, T. Maver, T. Mohan, K. Stana Kleinschek, U. Maver,

Development of multifunctional 3D printed bioscaffolds from polysaccharides and NiCu nanoparticles and their application, Appl. Surf. Sci. 488 (2019) 836–852.
[54] Vitaprint g-code generator. https://github.com/IRNAS/vitaprint-gcode-generator.
[55] N. Novak, M. Vesenjak, L. Krstulović-Opara, Z. Ren, Mechanical characterisation of auxetic cellular structures built from inverted tetrapods, Compos. Struct. 196 (2018) 96–107.
[56] M. Milojević, G. Harih, B. Vihar, J. Vajda, L. Gradišnik, T. Zidarič, K. Stana Kleinschek, U. Maver, T. Maver, Hybrid 3D printing of advanced hydrogel-based wound dressings with tailorable properties, Pharmaceutics 13 (4) (2021) 564.
[57] J. Vajda, B. Vihar, L. Ćurić, U. Maver, M. Vesenjak, P. Dubrovski, M. Milojević, Sr2+ vs. Ca2+ as post-processing ionic crosslinkers: Implications for 3D bioprinting of polysaccharide hydrogels in tissue engineering, J. Mater. Res. Technol. 23 (2023).
[58] C.H. Österreicher, M. Penz-Österreicher, S.I. Grivennikov, M. Guma, E. K. Koltsova, C. Datz, R. Sasik, G. Hardiman, M. Karin, D.A. Brenner, Fibroblast-specific protein 1 identifies an inflammatory subpopulation of macrophages in the liver, Proc. Natl. Acad. Sci. 108 (1) (2011) 308–313.
[59] S. Krishnamoorthy, B. Noorani, C. Xu, Effects of Encapsulated Cells on the Physical-Mechanical Properties and Microstructure of Gelatin Methacrylate Hydrogels, Int. J. Mol. Sci. 20 (20) (2019).
[60] A.M. Kloxin, C.J. Kloxin, C.N. Bowman, K.S. Anseth, Mechanical Properties of Cellularly Responsive Hydrogels and Their Experimental Determination, Adv. Mater. 22 (31) (2010) 3484–3494.
[61] S. Khetan, M. Guvendiren, W.R. Legant, D.M. Cohen, C.S. Chen, J.A. Burdick, Degradation-mediated cellular traction directs stem cell fate in covalently crosslinked three-dimensional hydrogels, Nat. Mater. 12 (5) (2013) 458–465.
[62] Y.A. Mørch, I. Donati, B.L. Strand, G. Skjåk-Braek, Effect of Ca2+, Ba2+, and Sr2 + on alginate microbeads, Biomacromolecules 7 (5) (2006) 1471–1480.
[63] O. Smidsrød, Molecular basis for some physical properties of alginates in the gel state, Faraday Discuss. Chem. Soc. 57 (0) (1974) 263–274.
[64] V. Karageorgiou, D. Kaplan, Porosity of 3D biomaterial scaffolds and osteogenesis, Biomaterials 26 (27) (2005) 5474–5491.
[65] D.W. Hutmacher, Scaffolds in tissue engineering bone and cartilage, Biomaterials 21 (24) (2000) 2529–2543.
[66] H.-Y. Liang, W.-K. Lee, J.-T. Hsu, J.-Y. Shih, T.-L. Ma, T. Vo, C.-W. Lee, M.-T. Cheng, I.T. Lee, Polycaprolactone in Bone Tissue Engineering: A Comprehensive Review of Innovations in Scaffold Fabrication and Surface Modifications, Journal of Functional Biomaterials 15 (2024) 243.
[67] V. Rahimkhoei, M. Padervand, M. Hedayat, F. Seidi, E.A. Dawi, A. Akbari, Biomedical applications of electrospun polycaprolactone-based carbohydrate polymers: A review, Int. J. Biol. Macromol. 253 (Pt 1) (2023) 126642.
[68] M. Woodruff, D. Hutmacher, The return of a forgotten polymer-polycaprolactone in the 21st century, Prog. Polym. Sci. 35 (2010).
[69] S. Homaeigohar, A.R. Boccaccini, Nature-derived and synthetic additives to poly (ε-caprolactone) nanofibrous systems for biomedicine; an updated overview, Front. Chem. Volume 9–2021 (2022).
[70] M.R. Williamson, R. Black, C. Kielty, PCL–PU composite vascular scaffold production for vascular tissue engineering: Attachment, proliferation and bioactivity of human vascular endothelial cells, Biomaterials 27 (19) (2006) 3608–3616.
[71] T. Mohan, F. Gürer, D. Bračič, F. Lackner, C. Nagaraj, U. Maver, L. Gradišnik, M. Finšgar, R. Kargl, K.S. Kleinschek, Functionalization of Polycaprolactone 3D Scaffolds with Hyaluronic Acid Glycine-Peptide Conjugates and Endothelial Cell Adhesion, Biomacromolecules 26 (3) (2025) 1771–1787.
[72] S.P. Bohari, D.W. Hukins, L.M. Grover, Effect of calcium alginate concentration on viability and proliferation of encapsulated fibroblasts, Biomed. Mater. Eng. 21 (3) (2011) 159–170.
[73] B.M. Whited, M.N. Rylander, The influence of electrospun scaffold topography on endothelial cell morphology, alignment, and adhesion in response to fluid flow, Biotechnol. Bioeng. 111(1) (2014) 184–95.
[74] M. Werner, S.B. Blanquer, S.P. Haimi, G. Korus, J.W. Dunlop, G.N. Duda, D.W. Grijpma, A. Petersen, Surface curvature differentially regulates stem cell migration and differentiation via altered attachment morphology and nuclear deformation, Adv Sci (Weinh) 4(2) (2017) 1600347, Adv. Sci.
[75] G. Altay, S. Tosi, M. García-Díaz, E. Martínez, Imaging the cell morphological response to 3D topography and curvature in engineered intestinal tissues, Front. Bioeng. Biotechnol. Volume 8–2020 (2020).
[76] T. Goodpaster, A. Legesse-Miller, M.R. Hameed, S.C. Aisner, J. Randolph-Habecker, H.A. Coller, An immunohistochemical method for identifying fibroblasts in formalin-fixed, paraffin-embedded tissue, J. Histochem. Cytochem. 56 (4) (2008) 347–358.
[77] S. Saraswati, S.M.W. Marrow, L.A. Watch, P.P. Young, Identification of a pro-angiogenic functional role for FSP1-positive fibroblast subtype in wound healing, Nat. Commun. 10 (1) (2019) 3027.
[78] M.F. Santolla, M. Talia, M. Maggiolini, S100A4 Is Involved in Stimulatory Effects Elicited by the FGF2/FGFR1 Signaling Pathway in Triple-Negative Breast Cancer (TNBC) Cells, Int. J. Mol. Sci. 22 (9) (2021).
[79] J.L. Hernández, L. Padilla, S. Dakhel, T. Coll, R. Hervas, J. Adan, M. Masa, F. Mitjans, J.M. Martinez, S. Coma, L. Rodríguez, V. Noé, C.J. Ciudad, F. Blasco, R. Messeguer, Therapeutic Targeting of Tumor Growth and Angiogenesis with a Novel Anti-S100A4 Monoclonal Antibody, PloS One 8 (9) (2013) e72480.
[80] S. Parvanian, L.S. Coelho-Rato, A.E. Patteson, J.E. Eriksson, Vimentin takes a hike - Emerging roles of extracellular vimentin in cancer and wound healing, Curr. Opin. Cell Biol. 85 (2023) 102246.
[81] N.C.A. van Engeland, F. Suarez Rodriguez, A. Rivero-Müller, T. Ristori, C. L. Duran, O.M.J.A. Stassen, D. Antfolk, R.C.H. Driessen, S. Ruohonen, S. T. Ruohonen, S. Nuutinen, E. Savontaus, S. Loerakker, K.J. Bayless, M. Sjöqvist, C. V.C. Bouten, J.E. Eriksson, C.M. Sahlgren, Vimentin regulates Notch signaling strength and arterial remodeling in response to hemodynamic stress, Sci. Rep. 9 (1) (2019) 12415.
[82] J.R. van Beijnum, E.J.M. Huijbers, K. van Loon, A. Blanas, P. Akbari, A. Roos, T. J. Wong, S.S. Denisov, T.M. Hackeng, C.R. Jimenez, P. Nowak-Sliwinska, A. W. Griffioen, Extracellular vimentin mimics VEGF and is a target for anti-angiogenic immunotherapy, Nat. Commun. 13 (1) (2022) 2842.
[83] R. Naomi, P.M. Ridzuan, H. Bahari, Current Insights into Collagen Type I, Polymers 13 (16) (2021) 2642.
[84] G.A. Rico-Llanos, S. Borrego-González, M. Moncayo-Donoso, J. Becerra, R. Visser, Collagen Type I Biomaterials as Scaffolds for Bone Tissue Engineering, Polymers 13 (4) (2021) 599.
[85] R. Sklenářová, N. Akla, M.J. Latorre, J. Ulrichová, J. Franková, Collagen as a biomaterial for skin and corneal wound healing, J. Funct. Biomater. 13 (4) (2022) 249.
[86] H. Kuivaniemi, G. Tromp, Type III collagen (COL3A1): Gene and protein structure, tissue distribution, and associated diseases, Gene 707 (2019) 151–171.
[87] S. Sharma, V.K. Rai, R.K. Narang, T.S. Markandeywar, Collagen-based formulations for wound healing: A literature review, Life Sci. 290 (2022) 120096.
[88] J.A. McDonald, D.G. Kelley, T.J. Broekelmann, Role of fibronectin in collagen deposition: Fab' to the gelatin-binding domain of fibronectin inhibits both fibronectin and collagen organization in fibroblast extracellular matrix, J. Cell Biol. 92 (2) (1982) 485–492.
[89] J. Sottile, F. Shi, I. Rublyevska, H.-Y. Chiang, J. Lust, J. Chandler, Fibronectin-dependent collagen I deposition modulates the cell response to fibronectin, Am. J. Phys. Cell Phys. 293 (6) (2007) C1934–C1946.
[90] H.N. Antoniades, T. Galanopoulos, J. Neville-Golden, C.P. Kiritsy, S.E. Lynch, Injury induces in vivo expression of platelet-derived growth factor (PDGF) and PDGF receptor mRNAs in skin epithelial cells and PDGF mRNA in connective tissue fibroblasts, Proc. Natl. Acad. Sci. U. S. A. 88 (2) (1991) 565–569.
[91] E. Brey, Vascularization: Regenerative Medicine and Tissue Engineering, Taylor & Francis Group, LLC, Boca Raton, FL, USA, 2015.
[92] D.C. Darland, P.A. D'Amore, TGF beta is required for the formation of capillary-like structures in three-dimensional cocultures of 10T1/2 and endothelial cells, Angiogenesis 4 (1) (2001) 11–20.
[93] D. Fukumura, R. Xavier, T. Sugiura, Y. Chen, E.C. Park, N. Lu, M. Selig, G. Nielsen, T. Taksir, R.K. Jain, B. Seed, Tumor induction of VEGF promoter activity in stromal cells, Cell 94 (6) (1998) 715–725.
[94] S. Kellouche, S. Mourah, A. Bonnefoy, D. Schoevaert, M.P. Podgorniak, F. Calvo, M.F. Hoylaerts, C. Legrand, C. Dosquet, Platelets, thrombospondin-1 and human dermal fibroblasts cooperate for stimulation of endothelial cell tubulogenesis through VEGF and PAI-1 regulation, Exp. Cell Res. 313 (3) (2007) 486–499.
[95] V. Paunescu, F.M. Bojin, C.A. Tatu, O.I. Gavriliuc, A. Rosca, A.T. Gruia, G. Tanasie, C. Bunu, D. Crisnic, M. Gherghiceanu, F.R. Tatu, C.S. Tatu, S. Vermesan, Tumour-associated fibroblasts and mesenchymal stem cells: more similarities than differences, J. Cell. Mol. Med. 15 (3) (2011) 635–646.
[96] T.L. Jenkins, D. Little, Synthetic scaffolds for musculoskeletal tissue engineering: cellular responses to fiber parameters, NPJ Regen. Med. 4 (1) (2019) 15.
[97] E.S. Lai, N.F. Huang, J.P. Cooke, G.G. Fuller, Aligned nanofibrillar collagen regulates endothelial organization and migration, Regen. Med. 7 (5) (2012) 649–661.
[98] J.T. Saunders, J.E. Schwarzbauer, Fibronectin matrix as a scaffold for procollagen proteinase binding and collagen processing, Mol. Biol. Cell 30 (17) (2019) 2218–2226.
[99] J.R. Libby, H. Royce, S.R. Walker, L. Li, The role of extracellular matrix in angiogenesis: Beyond adhesion and structure, Biomaterials and Biosystems 15 (2024) 100097.
[100] J. Sottile, D.C. Hocking, Fibronectin polymerization regulates the composition and stability of extracellular matrix fibrils and cell-matrix adhesions, Mol. Biol. Cell 13 (10) (2002) 3546–3559.
[101] M.E. Carnes, C.R. Gonyea, J.M. Coburn, G.D. Pins, A biomimetic approach to modulating the sustained release of fibroblast growth factor 2 from fibrin microthread scaffolds, Explor Biomat X 1 (2) (2024) 58–83.
[102] Y. Yu, Y. Leng, X. Song, J. Mu, L. Ma, L. Yin, Y. Zheng, Y. Lu, Y. Li, X. Qiu, H. Zhu, J. Li, D. Wang, Extracellular Matrix Stiffness Regulates Microvascular Stability by Controlling Endothelial Paracrine Signaling to Determine Pericyte Fate, Arterioscler. Thromb. Vasc. Biol. 43 (10) (2023) 1887–1899.
[103] R.A. Scott, E.W. Fowler, X. Jia, K.L. Kiick, R.E. Akins, Regulation of neovasculogenesis in co-cultures of aortic adventitial fibroblasts and microvascular endothelial cells by cell-cell interactions and TGF-β/ALK5 signaling, PloS One 15 (12) (2020) e0244243.
[104] J.M. Sorrell, M.A. Baber, A.I. Caplan, A self-assembled fibroblast-endothelial cell co-culture system that supports in vitro vasculogenesis by both human umbilical vein endothelial cells and human dermal microvascular endothelial cells, Cells Tissues Organs 186 (3) (2007) 157–168.
[105] A.K. Tamo, Nanocellulose-based hydrogels as versatile materials with interesting functional properties for tissue engineering applications, J. Mater. Chem. B 12 (32) (2024) 7692–7759.
[106] L. Lin, S. Jiang, J. Yang, J. Qiu, X. Jiao, X. Yue, X. Ke, G. Yang, L. Zhang, Application of 3D-bioprinted nanocellulose and cellulose derivative-based bio-inks in bone and cartilage tissue engineering, Int J Bioprint 9 (1) (2023) 637.
[107] B. Yi, Q. Xu, W. Liu, An overview of substrate stiffness guided cellular response and its applications in tissue regeneration, Bioact Mater 15 (2022) 82–102.